3D ENDOSCOPE BASED ON THE CONTROLLED ABERRATION METHOD

by

Mohan Xu

A Thesis Submitted to the Faculty of the

COLLEGE OF OPTICAL SCIENCE

In Partial Fulfillment of the Requirements

For the Degree of

MASTER OF SCIENCE

In the Graduate College

THE UNIVERSITY OF ARIZONA

2018

STATEMENT BY AUTHOR

The thesis titled 3D ENDOSCOPE BASED ON THE CONTROLLED ABERRATION METHOD prepared by Mohan Xu has been submitted in partial fulfillment of requirements for a master's degree at the University of Arizona and is deposited in the University Library to be made available to borrowers under rules of the Library.

SIGNED: Mohan Xu

APPROVAL BY THESIS DIRECTOR

This thesis has been approved on the date shown below:

Scott Tyo — Date: 6/MAY/2019

Professor of Optical Science

ACKNOWLEDGMENTS

I would like to express my gratitude to my advisor Dr. Scott Tyo for his continuous support of my research and writing and for his patience and professionalism. I could not complete this thesis without his understanding, tolerance, and help. He set an excellent example for me as a researcher and advisor.

I would like to thank Dr. Jim Schwiegerling for his guidance, insightful comments, and encouragement through my entire research process. My thanks also go to my committee member Dr. Arthur Gmitro for his feedback and help.

I would like to thank my parents Jing Yang and Fuhai Xu and my best friend Qiong Wei for the love and support which helped me went through the tough time in my life.

CONTENTS

LIST OF FIGURES:

LIST OF TABLES:

ABSTRACT

Surgeons use endoscopes to inspect the cavity of patient's body in the minimal invasive surgery. However, the conventional 2D endoscopes cannot offer depth information. Surgeons might overshoot the targets due to the lack of depth perception. So, it is essential to develop the 3D endoscopes to overcome this problem.

In current 3D imaging technologies, the stereo method and structured light method both require angle diversity. The controlled aberration method is a uniaxial depth measurement method. It only requires the projection pattern and the differential focus to implement depth measurement. It has potential to be applied in the endoscopic system.

This research aims to develop a 3D endoscope prototype based on the controlled aberration method and prove it can implement depth measurement. The first part of the work is a simulation study to prove that the controlled aberration method can be scaled down and applied to an endoscopic system for the depth measurement. Then the prototype design was discussed with each element in the projection path and imaging path of the system. Two depth measurement experiments were conducted. One is based on the miniature camera placed next to the projection path, another is based on an on-axis DSLR with diffuser screens. It used diffuser screens as "detector" and DSLR to capture the transmitted image on the screen. These experiement results indicate that endoscope prototype with controlled aberration method can implememnt depth measurement.

The mini camera configuration suffers from high distortion. It reduces the measurement accuracy. The DSLR configuration was developed to deal with the distortion problem. But the DSLR camera configuration is not applicable to the actual endoscope. Hence, the future work is to develop a controlled aberration prototype with co-axial projection and imaging path to capture the reflected pattern image of the scene and the optimization of the calibration and measurement processes for more accurate depth measurement.

CHAPTER 1

MOTIVATION

1.1 Introduction

The endoscope is a scope inserted into a body cavity to inspect and treat disorders. The endoscopic systems are named based on the required inspection area of the human body, such as the cystoscope for bladder, the gastroscope for stomach and the arthroscope for joints. In surgery, doctors use endoscopes to look inside the patient's body and use the cutting tool attached to the end of the endoscope to perform minimally invasive or non-invasive surgery. The minimally invasive surgery (MIS) with the endoscopic system has less damage to the healthy tissue, reduces the pain and infection risk, and shortens the recovery time and hospital stay. [1]

1.1.1 History of Endoscope

The first endoscope -called the "Lichtleiter"- was a light conductor developed by Philipp Bozzini in 1806. It conducted light to the inside of a patient's body and redirected it to the observer. This endoscope was a double aluminum tube equipped with strategically angled mirrors with candlelight for illumination. Nitze [2] was the first people who used the electrical light bulb as the light source. In 1936, the first semi-flexible endoscope was established by Georg Wolf [3]. After that, Basil Hirschowitz [4] and Larry Curtiss invented the first fiber optic endoscope in 1957. In 1960, Harold Hopkins [5] developed Rod lens endoscopy which led to a breakthrough of optical quality; it had significant improvements in the field of view, magnification, and focal length of the endoscope. The first video-endoscope was developed in 1983 by Welch Allyn [6]. Then, the emergence of high-resolution, high-quality video imaging chips enabled the 3D visualization of the 3D endoscope. [7]

1.1.2 Rigid Endoscope

Currently, the commercial endoscopes are either 'rigid' or 'flexible.' [7] Both 'rigid' and 'flexible' endoscopes have an illumination path and an imaging path. The illumination path is typically made of optical fibers. It brings light from the outside into the inside of the body cavity. The imaging path could image the area of interest from the tip of the insertion tube into the eyepiece and cameras outside of the body.

Rigid endoscopes use a rigid tube to house a stack of lenses and optical fibers (Figure 1.1). The imaging path consists of three optical elements: objective lenses, relay system, and an eyepiece or a focusing lens which present the image to a sensor. To avoid light loss, the designers made all those three optical elements telecentric: the objective lenses are telecentric in the object space, the eyepiece is telecentric in image space, the relay system is double telecentric.

There are three different kinds of relay systems for the rigid endoscope. (Figure 1.2[7, 8]) One is the conventional relay system; one is the rod lenses which firstly developed by Hopkins, another is the GRIN lens relay system. For the conventional relay system, all the lenses are thin. When we mount those thin lenses inside of a rigid tube, the clear aperture of each piece is small which will end up with low light throughput. [9]

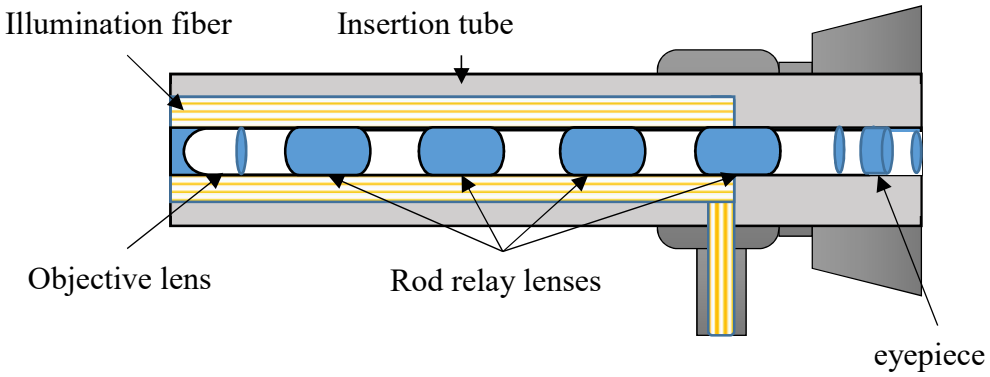

Figure 1.1 Scheme of rigid endoscope with rod relay lenses

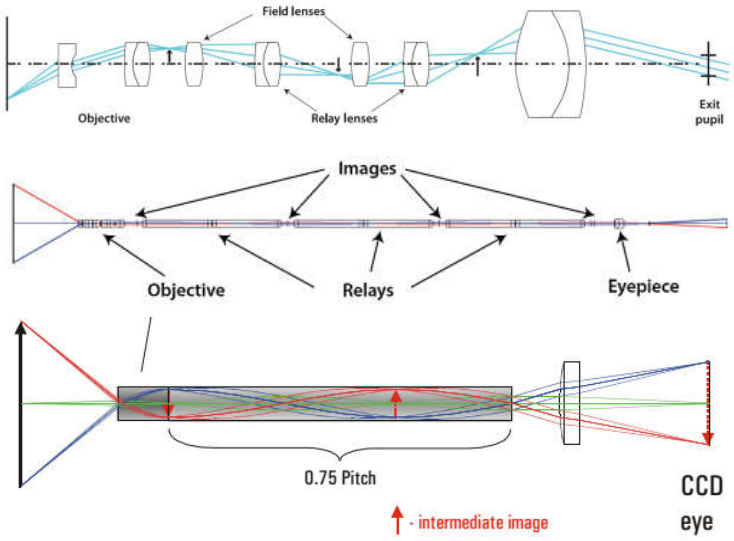

Figure 1.2 The top figure is Rigid endoscope optics with conventional relay lenses. (Courtesy Dr. D. C. Leiner). The middle figure is Rigid endoscope optics with Hopkins rod lenses as relay (Courtesy Dr. D. C. Leiner). The bottom figure is Gradient Index lenses endoscope optics. (Courtesy GRINTECH)

The conventional relay system uses air as the medium between relay lens and the field lens. The Hopkins rod lenses relay system uses glass as the medium. So, the relay system becomes into several rod lenses. The rod lenses relay system increases the refractive index of the medium and enlarges the clear aperture of the relay optics. In this sense, this relay system has higher light throughput than the conventional relay with the same outside diameter tube.

The GRIN lens relay system has larger NA and could be fabricated as small diameter. It has planar surface which leads to the advantage of low-cost and easy assembly. Also, the GRIN relay system has larger optical invariant than the conventional relay system in the same diameter. However, it suffers from chromatic aberration.

Figure 1.3 Olympus flexible GI endoscope GIF-HQ190. (Left) distal end enlarged. (right) (Courtesy Olympus)

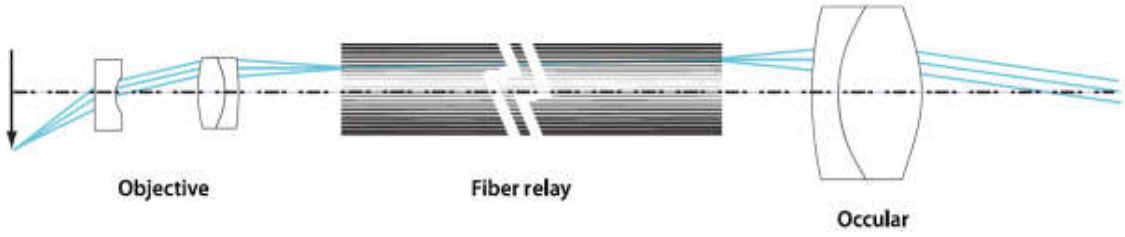

Figure 1.4 Flexible endoscope optics (Courtesy Dr. D. C. Leiner)

1.1.3 Flexible Endoscope

The flexible endoscope is another commonly used endoscopic system. Figure 1.3 [10] shows a flexible endoscope. It includes a flexible insertion tube, control handle, light tube guide, and camera. The flexible insertion tube is an essential part of this device. It contains the illumination channel, imaging channel, water channel and instrument channel. When in use the light tube guide is connected to a light source, and the flexible insertion tube is inserted inside of a patients' body. The flexible endoscope is constructed with the illumination path and the image path as well. For the image path, typically it either uses fiber optics as the relay system (Figure 1.4[7]) or uses a miniature video camera with a corresponding camera lens at the tip of the endoscope to directly capture the image of the test scene.

1.2 Specification of Current 2D Endoscopic Systems

There are several standard specifications of the commercial 2D endoscopic system. Those are the direction of view (DOV), the field of view (FOV), depth of field (DOF). Insertion tube diameter (ITD), working length (WL), image resolution. From the Table 1.1, we can tell the image channel diameter is generally from 1mm to 4mm in rigid endoscopes, and the FOV is from 90° to 170°

Table 1.1 Specification of current 2D endoscopes

Brand	Type	Model	IT Dia	Channel	FOV	DOV	DOF	WL	Resolution
Olympus	Gastroscopes	GIF-HQ190	9.9mm	2.8mm	140°	Forward	Normal 5-100 mm Near 2-6 mm	1030mm	1280×1024
	Gastroscopes	GIF-H190	9.2mm	2.8mm	140°	Forward	2-100mm	1030mm	1280×1024
	Gastroscopes	GIF-XP190N	5.8mm	2.2mm	140°	Forward	3-100mm	1100mm	1280×1024
	Colonoscope	PCF–PH190L	9.5mm	3.2mm	140°	Forward	2-100mm	1680mm	1280×1024
	Colonoscope	PCF–H190L	11.5mm	3.2mm	170°	Forward	2-100mm	1680mm	1280×1024
	Colonoscope	CF–HQ190L	12.8mm	3.7mm	Normal focus:170° Near focus 160°	Forward	Normal focus 5-100mm Near focus 2-6mm	1680mm	1280×1024
	Cystoscope	CYF-VH	5.5mm	2.2mm	120°	Forward	3-50mm	380mm	-
PENTAX	Gastroscope	EG 2990i	9.8mm	2.8mm	140°	Forward	5–100mm	1050mm	1920×1080
		EG 2790i	9.0mm	2.8mm	140°	Forward	4-100mm	1050mm	1920×1080
	Colonoscope	EC 3890Li	13.2mm	3.8mm	140°	Forward	4-100mm	1700mm	1920×1080
		EC 3490Li	11.6mm	3.2mm	140°	Forward	4-100mm	1700mm	1920×1080
	Small Bowel Endoscope	VSB-3430K	11.6mm	3.8mm	140°	Forward	-	2200mm	-
	Duodenoscopes	ED-3490TK	11.6mm	4.2mm	100°	-	-	1250mm	-
	Choledochofiberscope	FCP-9P	3.1mm	1.2mm	90° (Air) 40° (Water)	-	-	1900mm	-
	Cystoscope	ECY-1570K	5.1mm	2.0mm	120° (air)	-	-	400mm	-

					80° (water)				
	Ureteroscope	FUR-9RBS	3.0mm	1.2mm	90° (air) 64° (water)	-	-	700mm	-
	Bronchoscopes	EB-1170K	3.7mm	1.2mm	120°	-	-	600mm	-
Fujinon	Gastroscope	EG 590 WR	10.8mm	2.8mm	140°	Forward	4-100mm	1100mm	1280×1080
FUJIFILM	Gastroscopes	EC-600HL	12.8mm	4.2mm	170°	Forward	2-100mm	1690mm	-
Olympus	Laparoscope-rigid	WA50052A	5.4mm	-	80°	30°	12-200mm	302mm	1280×1024
Olympus	Laparoscope-rigid	WA53000A	10mm	-	75°	Forward	-	316mm	-
Olympus	Cystoscopes-rigid	A4605A	4mm	-	30°	-	-	-	-
ACMI	Cystoscopes-rigid	M3-70	4mm	-	70°	-	-	-	-
Stryker	Laparoscope-rigid	502-555-030	5mm	-	75°	30°	-	300mm	-
KARL STORZ	Laparoscope-rigid	26008AA	2mm	-	-	Forward	-	260mm	-

1.3 Introduction of 3D Endoscope

A 2D endoscope only provides monoscopic visual cues, such as overlapping, size familiarity, and texture gradients, so the surgeon must mentally construct the patient's three-dimensional anatomy without the depth information. However, surgeons might misjudge the object depth and overshoot the targets due to the lack of depth perception. [1] After the evaluation of 252 cases of laparoscopic cholecystectomy, researchers find out that the depth misperception caused 97% of the accidents. [11] To overcome the no depth cue problem, people started developing the three-dimensional endoscopic systems during the early 1990s.

One of the most popular commercial 3D endoscopes is da Vinci® Surgical System. This surgical system consists of four components: a surgeon console where the surgeons sit while operating; one patient-side cart is where the patient has positioned during surgery; a full range of Endowrist instruments and one vision system with a high-definition 3D endoscope and image processing equipment that provides stereo images of the patient's anatomy.

This 3D endoscope is a flexible tube with two separated cameras at the tip. (Figure 1.5[12]) It can provide a stereo view of the patient's anatomy. The principle for depth measurement of the stereo endoscope is the triangulation method. The details of this method will be discussed in the literature review section.

Figure 1.5 Tip of the Da Vinci stereo endoscope (Courtesy Intuitive Surgical)

1.4 Comparison: 3D versus 2D Endoscopic System

3D endoscope system could offer the depth information. However, whether the 3D endoscopic system has better performance than the 2D system is still a question. There are many studies about the comparison of the 2D endoscopic system and 3D endoscopic system in three different aspects: The first one is the physical performance such as the operation time and the accuracy. The second aspect is the subject evaluation. The third one is the adverse effect.

Table 1.2 shows the study of the comparison between the 3D and the 2D endoscopic system of the modern commercial products from 2008 to 2015. Those studies all show that the 3D endoscopic system has the same or better performance in operation time and the accuracy in both the novice and the experienced group. Also, both the novice and the experienced group prefer to use 3D endoscopic systems. For the adverse effect, the 3D endoscopic system might cause dizziness. However, from most of the study, the adverse effect of the 3D endoscope is not dramatically worse than the 2D system.

Table 1.1 Study characteristics of the comparison of 3D versus 2D endoscopic system

Study	Platform		Conclusion			
	2D	3D	Time	Accuracy	Subject evaluation	Adverse Effect
Kong et al.(2010)[13]	Olympus 10 mm, 0° A5294A	Wasol camera system prototype	2D ≈ 3D in both novice and experienced group	3D >2D in the novice group 2D ≈ 3D the experienced group	3D>2D in both novice and experienced group	
Storz et al.(2012)[14]	Richard Wolf GmbH, 2D mode	Richard Wolf GmbH, 3D mode	3D > 2D in both novice and experienced group	3D>2D in both novice and experienced group		
Usta et al.(2014)[15]	Viking 2DHD	Viking 3DHD	3D > 2D in both novice and experienced group	3D>2D in both novice and experienced group	3D>2D in the novice group 3D≈2D the experienced group	2D ≈ 3D in both novice and experienced group
Smith et al.(2014) [16]	Endo-Stereovision 2DHD	Endo-Stereovision 3DHD	3D>2D the experienced group	3D>2D experienced group	3D>2D experienced group	2D ≈ 3D experienced group
Alaraimi et al. (2014) [17]	Sony camcorder 2DHD	Sony camcorder 3DHD	2D ≈ 3D in the novice group	3D>2D in the novice group	2D ≈ 3D in the novice group	3D>2D in the novice group
Lusch et al.(2013) [18]	Karl Storz 2DHD	Karl Storz 3DHD	3D>2D In both novice and experienced group	3D>2D In both novice and experienced group	3D>2D In both novice and experienced group	2D ≈ 3D in both novice and experienced group
Tanagho et al. (2012) [19]	Viking NR	Viking 3DHD	3D>2D	3D>2D	3D>2D	2D ≈ 3D

			In both novice and experienced group	In both novice and experienced group	In both novice and experienced group	in both novice and experienced group
Honeck et al. (2012) [20]	Karl Storz 2DHD	Einstein Schölly 3DHD	2D ≈ 3D In both novice and experienced group	3D>2D In both novice and experienced group	3D>2D In both novice and experienced group	
Ko et al. (2014) [21]	Olympus EndoEye flex 2DHD	Olympus EndoEye flex 3DHD	3D>2D For particular task in both novice and experienced group		3D>2D In both novice and experienced group	2D ≈ 3D For nausea, headache and so on, 2D>3D for dizziness
Gómez-Gómez et al. (2015)[22]	Karl Storz 2DHD	Karl Storz TipCam 3DHD	3D>2D In novice group	3D>2D In novice group	3D>2D In novice group	2D>3D In novice group
Özsoy et al. (2015) [23]	Karl Storz 2DHD	Karl Storz TipCam 3DHD		3D>2D In novice and intermediate group	3D>2D In novice and intermediate group	
Bittner et al. (2008) [24]	Viking	Viking	3D≈2D	3D≈2D	3D>2D	

*3D>2D means 3D endoscope has better performance. 3D≈2D means the not much difference between the performance of the 3D system and 2D system. NR=not report

1.5 Literature Review of the Current 3D Endoscopes

The performance of 3D endoscopes is better than or equivalent to 2D systems. It potentially could shorten the operation time and increase the surgery accuracy. In this sense, people developed a lot of 3D endoscopic systems in recent years. The current available 3D surface imaging techniques in endoscopy can be classified into three categories, stereo endoscope, structured light endoscope and the uniaxial 3D imaging endoscope. [2] In this section, the details of each technology and its advantages and limitations will be discussed.

1.5.1 Stereo Endoscope

Stereo endoscope uses a pair of image sensors or two separate channels of optics to achieve binocular stereo images of the target scene. Those stereo images could present the binocular disparity which is a primary visual cue for the 3D rebuilding of human vision. The stereo images with head-mounted displays could offer natural sight for the surgeons in experiencing the depth of the target. [1]

The DaVinci surgical robotic surgery system is one of the most promising commercial stereo endoscopes. It has two separated cameras at the tip to capture the stereo image pairs. Figure 1.6 shows the scheme of the 3D image acquisition of a dual optics system. [25] There are two optical paths in the endoscopic system. Each of the optical path works with its corresponding objective lenses to image the target scene into the base unit. Inside of the base unit, there are specially designed prisms and lenses to adjust the dual optical paths to image onto the dual CCD sensors. Those two images can be used to generate the stereo view of the target object.

The stereo endoscope can only offer stereo image pairs. If the user wants to have the quantitative 3D measurement, the 3D reconstruction algorithm is required here. All those algorithms are based on the triangulation method. Figure 1.7 shows the basic concept of the triangulation method. L is

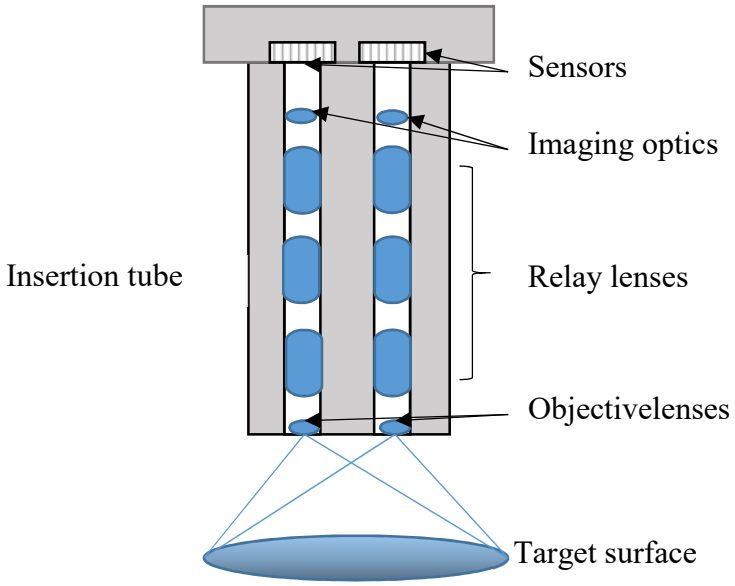

Figure 1.6 Illustration of the stereo endoscope

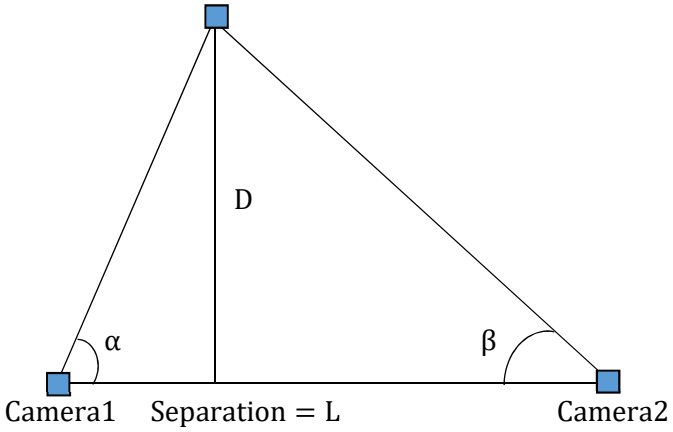

Figure 1.7 Triangulation method for distance calculation

the separation between two sensors. The orientation angle for those two cameras are α and β correspondingly, the object distance D is:

$$D = \frac{L}{\frac{1}{\tan\alpha} + \frac{1}{\tan\beta}} \tag{1.1}$$

1.5.2 Structured Light Endoscope

The stereo endoscopes can offer the stereo image pairs to help the surgeons to create the binocular depth cue. It either uses the dual cameras or the dual optical channels corresponding to the different sensors. The stereo endoscope uses the triangulation method for depth measurement. Another method based on the triangulation method is the structured light technology. [26]

The structured light endoscope could achieve the entire field quantitative 3D data acquisition with a specially designed 2D spatially-varying intensity pattern for illumination and an off-axis camera for capturing. When the test surface is planar, the acquired image shows a similar pattern as the illumination pattern; However, when the test surface has depth variation, the captured image differs from the illuminated pattern. Since the projected pattern is coded, it is easy to find the corresponding point on the image plane for each projected point. Then with the triangulation calculation, we can extract the accurate 3D surface information. Figure 1.8 is the basic concept for the depth measurement of the structured light method.[26] Assume the center of the captured

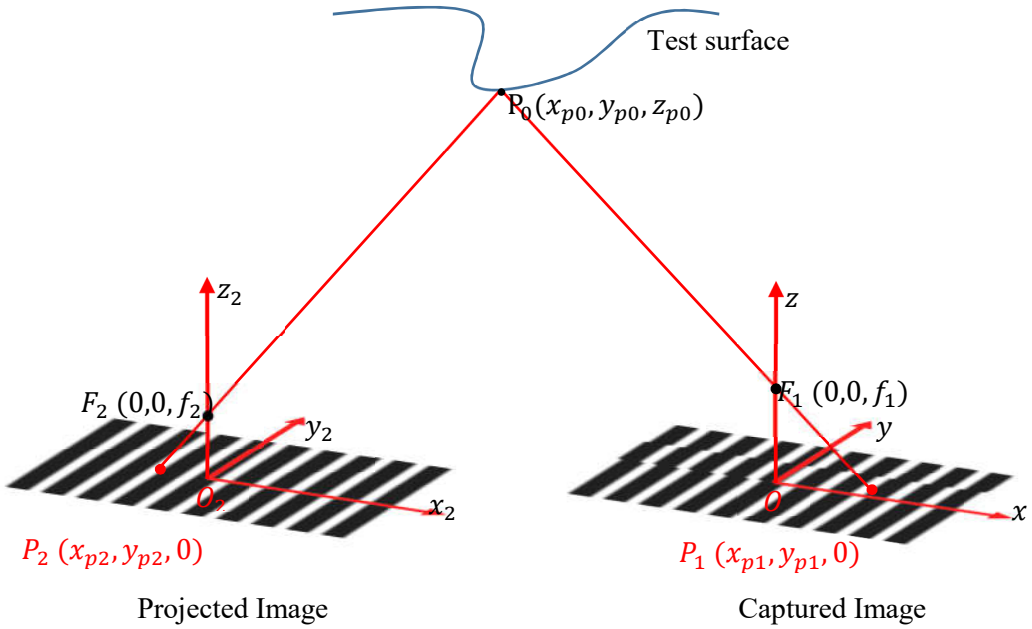

Figure 1.8 Depth measurement with structured light

image locates at the origin of the global coordinate O. For a test object $P_0(x_{p0}, y_{p0}, x_{p0})^T$ the corresponding point on projection plane is P_2 and on capture image plane point is P_1. Assume the coordinate $O_2 = [x_2\ y_2\ z_2]^T$ of projected image plane has the same orientation as golabl coordinate O. Hence the focal piont F_2 locates at $(x_2, y_2, z_2 + f_2)^T$ in global coordinate O and P_2 locates at $(x_{p2} + x_2, y_{p2} + x_2, z_2)$ in global coordinate O . The point P_2 on perojection image plane be projected onto object point P_0 and be captured onto image plane as point P_1, then it has

$$P_2 = F_2 + \beta(P_0 - F_2) \tag{1.2}$$

$$P_1 = F_1 + \alpha(P_0 - F_1) \tag{1.3}$$

Rewrite the equation (1.2) and (1.3) in the matrix form and simplify it, then it gives

$$z_{p0} = \frac{f_1 f_2}{f_1 x_{p_2} - f_2 x_{p1}}\left(x_2 + x_{p2} - x_{p1} + \frac{z_2\, x_{p2}}{f_2}\right) \tag{1.4}$$

$$z_{p0} = \frac{f_1 f_2}{f_1 y_{p2} - f_2 y_{p1}}\left(y_2 + y_{p2} - y_{p1} + \frac{z_2 y_{p2}}{f_2}\right) \tag{1.5}$$

The calibration process will determine f_1, f_2, x_2, y_2, z_2. Then with the object corresponding point on projection (x_{p2}, y_{p2}) and on image plane (x_{p1}, y_{p1}), it is easy to calculate the object depth z_{p0} based on equation (1.4) and (1.5). The details about the calibration processing can be found in Batlle, J (1998) [26].

One example is a miniaturized structured light surface shape measurement system for the minimally invasive surgery. [27] It used a structured lighting probe for illumination and a standard endoscope camera for imaging. The probe is fiber-based and has 1.7 mm diameter. Each of the projected point is labeled by a specific wavelength. When captured by the endoscope camera, each point is segmented by its RGB value while its 3D coordinate is calculated after the camera calibration.

A significant advantage of the structured light method is that it can retain high spatial resolution image since it uses a conventional imaging device. The disadvantage is it requires a large angle

diversity between the projection path and imaging path. In this sense, the current systems tend to be used in the macroscopic imaging rather than in endoscopy.

1.5.3 Uniaxial 3D Imaging Endoscope

Both the stereo endoscope and the structured light endoscope requires angle diversity. The stereo endoscope needs two distinct imaging paths while the structured light endoscope uses off-axis imaging path. The separation of optical axis could lead to some significant problems. One is the large diameter size of the endoscope insertion tube; another is that the off-axis configuration has problems measuring depth holes and steep height and shadow portions. The depth resolution is also related to the baseline separation. The uniaxial endoscopes have been proposed to overcome those problems. [28] The uniaxial endoscopes methods include the time-of-flight method, defocus and controlled aberration method, to name a few.

1.5.3.1 Time of Flight (ToF) 3D Endoscope

Time-of-flight method has been used for distance measurement for decades. It implements the depth measurement by illuminating the scene with a controlled laser or LED source and then analyzing the reflected light. The ToF systems use either the pulsed light modulation or the continuous- waves light modulation. [29] The pulsed-light camera uses the time difference Δt between the emission signal and the reflected signal by the object to measure the depth (Figure 1.9). With the light speed c, the distance d between the sensor and object can be expressed as

$$d = \Delta t \times \frac{c}{2} \tag{1.6}$$

The continuous - wave modulated light camera use the phase difference between the emitted and received signals for depth measurement. With the known modulation frequency f , the phase

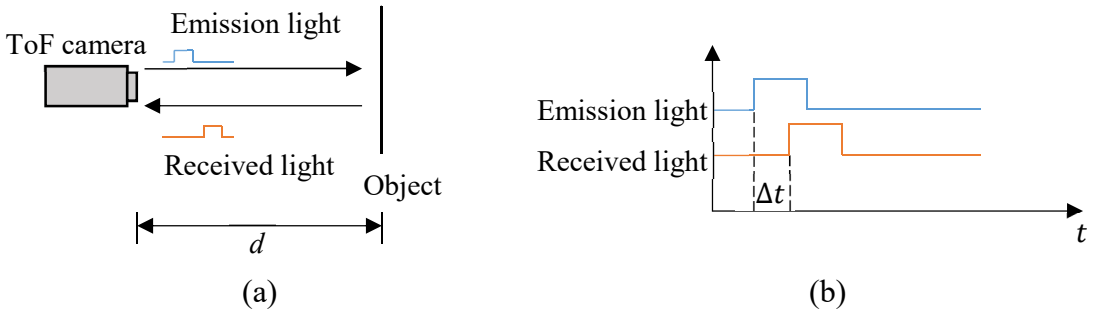

Figure 1.9 ToF distance measurement principle with the pulsed-light camera

difference ϕ is directly related to the distance d. The phase difference can be calculated by the cross- correlation between the emitted and received signals. Use the sinusoidal signal for instance. The emitted signal is $s(t) = a\cos(2\pi ft)$; The received signal is $r(t) = A\cos\big(2\pi f(t-\tau)\big) + B$ Then the cross-correlation between those two signals is

$$C(x) = \lim_{T\to\infty}\frac{1}{T}\int_{-T/2}^{T/2} r(t)s(t+x)dt = \frac{aA}{2}\cos(2\pi f\tau + 2\pi fx) + B \tag{1.7}$$

The Phase difference is $\phi = 2\pi f\tau$. A is the amplitude of the received signal. B is the offset component form the ambient illumination. Set $\psi = 2\pi fx$, and calculate the values $C(\psi)$ for $\psi_0 = 0°, \psi_1 = 90°, \psi_2 = 180°, \psi_3 = 270°$. The phase difference ϕ is

$$\phi = 2\pi f\tau = \arctan\left(\frac{C(\psi_3) - C(\psi_1)}{C(\psi_0) - C(\psi_1)}\right) \tag{1.8}$$

Then the depth d is

$$d = \frac{1}{2}c\tau = \frac{c}{2f}\frac{\phi}{2\pi} \tag{1.9}$$

The phase difference ϕ is defined up to 2π. The actual depth is calculated with the unwrapped phase difference.

One example of the ToF endoscope is accomplished with the off-the-shelf ToF continuous-wave modulated camera (PMD 3k-S from PMDTec GmbH) and endoscope optics. The emitted light is a sinusoidal signal with a known frequency. The prototype can achieve the depth measurement precision of 0.89 mm at 20 fps with 3072 pixels of the depth information. [30]

1.5.3.2 Defocus 3D Endoscope

Depth from defocus is another uniaxial depth measurement method. This method is based on the image contrast change along the optical axis. Figure 1.10 shows the principle of the defocus 3D measurement method. In this measurement, the system projects a sinusoidal pattern onto the object and measure the contrast of the reflected pattern image. The reflected pattern contrast varies along the optical axis approximately as Bessel distribution. The highest contrast locates at the focal plane. Then by measuring the contrast of each pixel, the user can get the depth information at this pixel. One 3D defocus endoscope prototype example is made with varifocal liquid crystal lens.[31] This lens could change focal length continuously by changing the shape of the lens from concave to convex with the liquid pressure. The defocus endoscope with varifocal liquid crystal lens could expand the depth measurement range.

The captured image has the intensity $\mathrm{I_i}$ for pixel locate at (x,y) can be expressed as the combination of average intensity $\mathrm{I_0}$, contrast V(x,y), and initial phase $\phi(\mathrm{x},\mathrm{y})$ and the shifted phase $\delta_\mathrm{i}(0°, 90°, 180°, 270°)$ of the sinusoidal pattern. The captured intensity is:

$$\mathrm{I_i} = I_0(1 + V(x,y)\ \cdot \cos(\phi(x,y) + \delta_i)) \tag{1.10}$$

In this sense, the contrast can be calculated by four steps-phase shift method:

$$\mathrm{V(x,y)} = \frac{2\sqrt{(I_{0°} - I_{18\ 0}{}_{9})^2 + (I_{90°} - I_{27\ 0}{}_{9})^2}}{I_{0°} + I_{90°} + I_{18\ 0°} + I_{27\ 0°}} \tag{1.11}$$

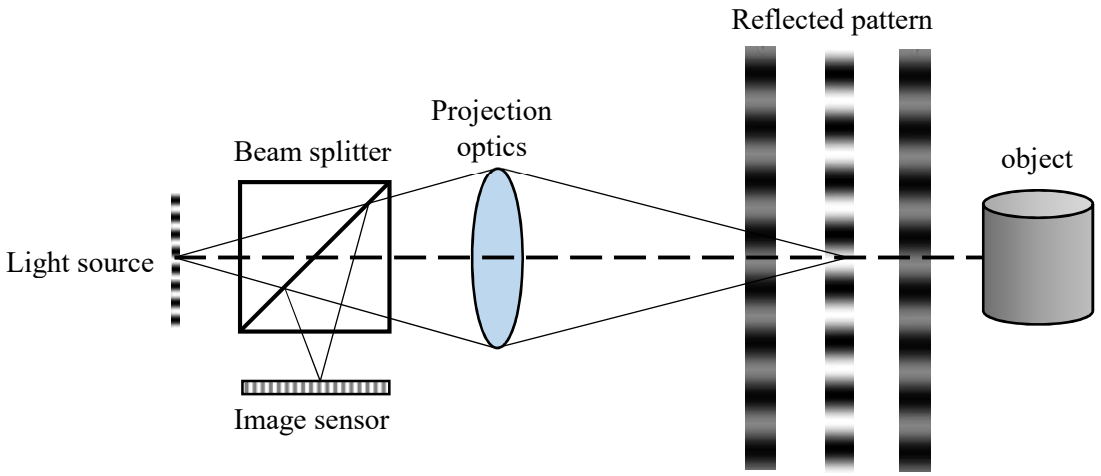

Figure 1.10 Principle of the defocus 3D measurement method

The defocus method is uniaxial, and it can use the same optical design as the conventional endoscope. However, it has limitations in measuring the low contrast object.

1.5.4 The Advantages and Limitations of the Current 3D Endoscopes

Table 1.3 shows the advantages and the limitations of the current 3D imaging methods in endoscopy. Both the stereo and structured light methods are low cost, but they require angle diversity for depth measurement. The Time-of-Flight method offers excellent 3D imaging information over a long distance, but the frame rate is low, and the Time-of-Flight cameras are expensive. Both the Defocus and controlled aberration of the astigmatic pattern method can achieve depth measurement with no angle diversity. The defocus method is computational; it does not require any change in optical design. However, it is difficult to apply the depth method to the low contrast object measurement. To overcome this problem, we proposed the use of controlled aberration method in the 3D imaging endoscopy. This method only requires the projection pattern and the differential focus.

Table 1.3 The advantages and limitations of the current 3D imaging methods in endoscopy

	Stereo	Structured light	Uniaxial		
			Time of Flight	Defocus	Controlled aberration
Incoherent Illumination	Yes	Yes	No	Yes	Yes
No Angle Diversity Required	No	No	Yes	Yes	Yes
Frame rate	high	low	low	medium	medium
Retain 2D image resolution	Yes	Yes	No	Yes	Yes
Inexpensive	Yes	Yes	No	Yes	Yes

1.6 Controlled Aberration Method

The stereo endoscope and the structured light endoscope both require the baseline separation. This separation will lead to the larger insertion tube diameter and inaccurate measurement for steep objects. The uniaxial 3D methods could deal with those problems. However, the Time-of-Flight cameras are expensive, and the defocus method has limitations in measuring the low contrast objects. Therefore, we can apply the controlled aberration method in an endoscope for depth measurement.

1.6.1 Concept for Controlled Aberration Method for Depth Measurement

The controlled aberration depth measurement method requires a projection pattern and differential focus. A cylinder lens is added in the illumination path to generate astigmatism. The aberrated pattern is projected on the test scene and is captured for depth measurement.

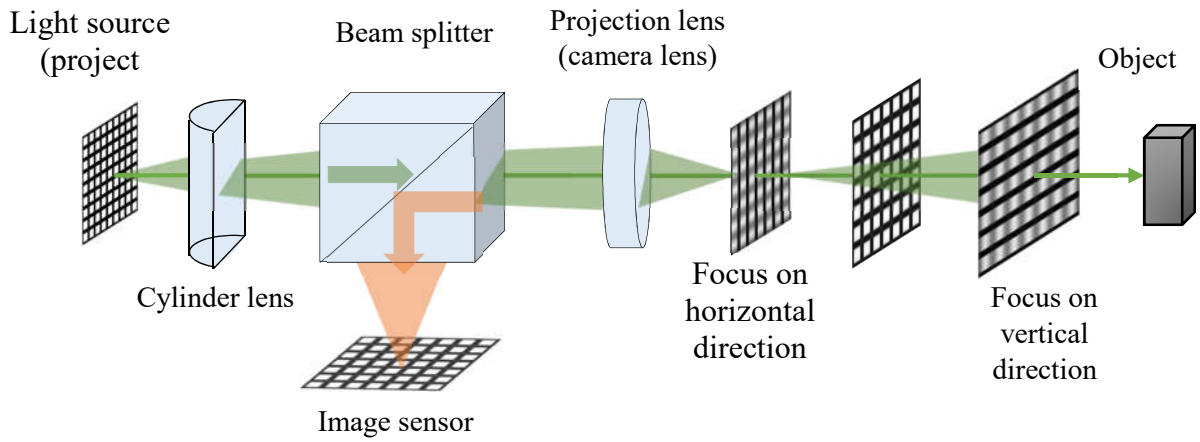

Figure 1.11 Principle of the controlled aberration depth measurement method

Figure 1.11 shows the principle of the controlled aberration depth measurement method. The controlled aberration method is uniaxial. In this configuration, we can use a beam splitter to combine the projection path and the imaging path. The cylinder lens is in front of the beam splitter to add astigmatism in the illumination path without changing the imaging path. The projection lens here also works as the objective lens. In this set-up, the cylinder lens brings extra power in the horizontal direction. In this sense, the projected grid pattern focusses in the horizontal direction first, then focus in the vertical direction. For each direction, the image contrast varies along the optical axis and reaches its maximum at its the focal plane. So, the image contrast ratio of the horizontal direction and vertical direction also varies along the optical axis as a monotonic function in between the horizontal focal plane and vertical focal plane. In the measurement, by capturing the reflected pattern image from the test scene and measuring the contrast ratio of the horizontal direction and vertical direction, we can get the depth information.

One depth measurement with controlled aberration was implemented with a projector system with astigmatic focus and a commercial digital camera close to the projector. [32] In this measurement, the contrast was being calculated with the wavelet algorithm. The wavelet algorithm could extract the frequency information corresponding to the pattern frequency while keeping the location information. The level and the filter of the wavelet were chosen based on the projected pattern.

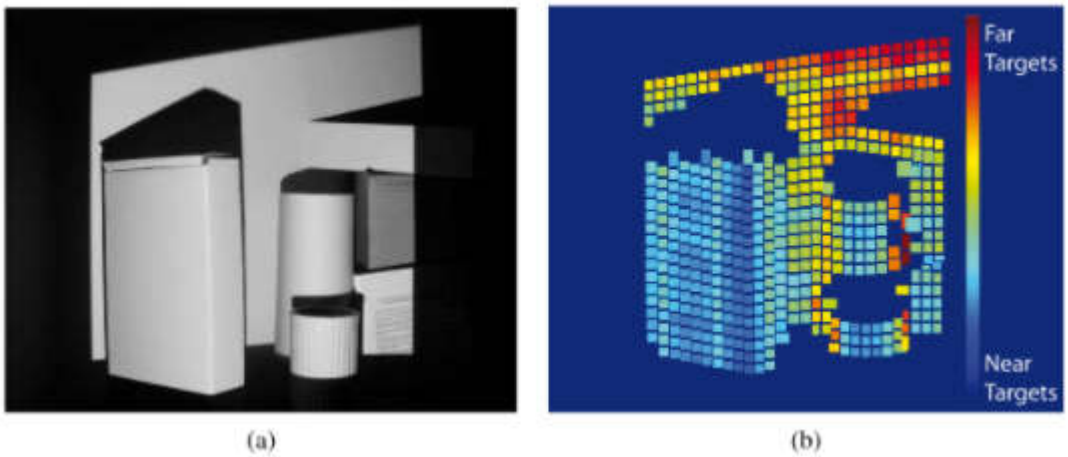

Figure 1.12 (a) The original 2D image (b) depth map [Reprinted] with permission from [32] , [OSA]. (G. C. Birch, J. S. Tyo, and J. Schwiegerling, "Depth measurements through controlled aberrations of projected patterns," Optics express 20, 6561 (2012).)

With calibration, this system could achieve approximately 1- inch depth resolution. Figure 1.12 shows the original image (a) and the labeled depth map (b).

1.7 Conclusion

In this chapter, the first part is about the history of the endoscope development and the introduction to the structure of the rigid and flexible endoscopes. For the current commercial 2D endoscopes, the image channel diameter ranges from 1.2mm to 4mm and the FOV is for 90° to 140°. 3D endoscope is an option to overcome the lack of depth information problem of the 2D endoscope and research shows the 3D endoscope have better or equivalent performance than the 2D endoscopes. The literature review is about the popular 3D endoscopes such as the stereo endoscope, structured light depth measurement endoscope as well as the un-axial endoscopes – ToF, defocus depth measurement and the controlled aberration endoscope. Among those technologies, the controlled aberration endoscope has some advantages. For instance, it doesn't require the angle diversity which leads to a small insertion tube; It is low cost and could maintain the high-resolution 2D image. In this sense, the controlled aberration 3D endoscope is essential for improving the MIS surgeries as well as overcoming the limitations in the other 3D imaging methods.

In this thesis, a simulation study has been implemented to prove that the controlled aberration method can be applied in the endoscopic scale. Then a controlled aberration endoscope prototype was built, and depth measurement experiments were conducted based on the prototype. Chapter 2 present a simulation of the astigmatismic projection system in the endoscopic size to prove that the depth information of the test scene is encoded in the contrast ratio of the pattern image. In this simulation, the influences of field, projection pattern frequency as well as the illumination wavelength were discussed. In chapter 3, I talk about the strategy of the controlled aberration endoscope prototype design as well as the final choice for each element. The most critical part of the prototype is the illumination path. It projects the aberrated pattern onto the test scene. The main construction parts are the light source and coupling lens, relay system, and the projection system.

In chapter 4, two experiements were conducted based on the controlled aberration prototype with a mini-camera and an on-axis DSLR camera. The mini-camera suffers from the low-resolution and high distortion, so it cannot achieve the accurate calibration for the depth measurement. So, the experiment setup is only based on step object and the results prove the contrast ratio at the different depth has a significant difference. To overcome the high distortion problem in mini camera, I also discussed the configuration based on diffuser screens and an on-axis DSLR camera. In this configuration , the diffuser screens act as “detector” and the DSLR camera capture the image on the diffuser screen for measurement. In this session, the calibration process is presented first; then the depth measurement is done with two separated diffuser screens at different distances.

Chapter 5 is about the future work and conclustion. The DLSR configuration is not applicable in the actual endoscope, the future works include developing compact ptoryprw with the projection path and illumination path in th e same side.

CHAPTER 2

SIMULATION STUDY

2.1 Introduction

The principle of the controlled aberration method was introduced in chapter1; This chapter presents the simulation study to prove that the controlled aberration method can be scaled down and applied to an endoscopic system for the depth measurement.

2.2 Simulation Goal

In this study, we will simulate a projection system with astigmatism in endoscopic scale. The goal is to find out the contrast ratio change along the optical axis in its image space. The controlled aberration endoscope requires a projection with astigmatism and an imaging path. In the illumination path, we add a cylinder lens to create astigmatic focus. This cylinder lens produces the contrast difference between horizontal and vertical direction. In this sense, in this simulation we neglect the imaging path and relay optics from the illumination path, only simulate the projection lens with cylinder lens.

The image contrast shows the difference between the brightest and darkest of an image. Set I_{max} as the maximum internsity , I_{min} is the minimum intensity of the image. The Michelson Contrast is

$$\text{Constrast} = \frac{I_{max} - I_{min}}{I_{max} + I_{min}} \tag{2.1}$$

In this simulation, the image contrast is calculated by measuring the MTF from the zemax model of the projection system. The MTF is the modulation transfer function of an optical system. It is

the measurement of the optical system ability to transfer contrast at a specific frequency from the object to the image. For a grating object with contrast equals to 1 and frequency f_0, the contrast for its image is the MTF value at the frequency f_0 .(Figure 2.1)

$$\text{MTF(spatial frequency } f_0) = \frac{\text{Image contrast for spatial frequency } f_0}{\text{Object contrast for spatial frequency } f_0} \tag{2.2}$$

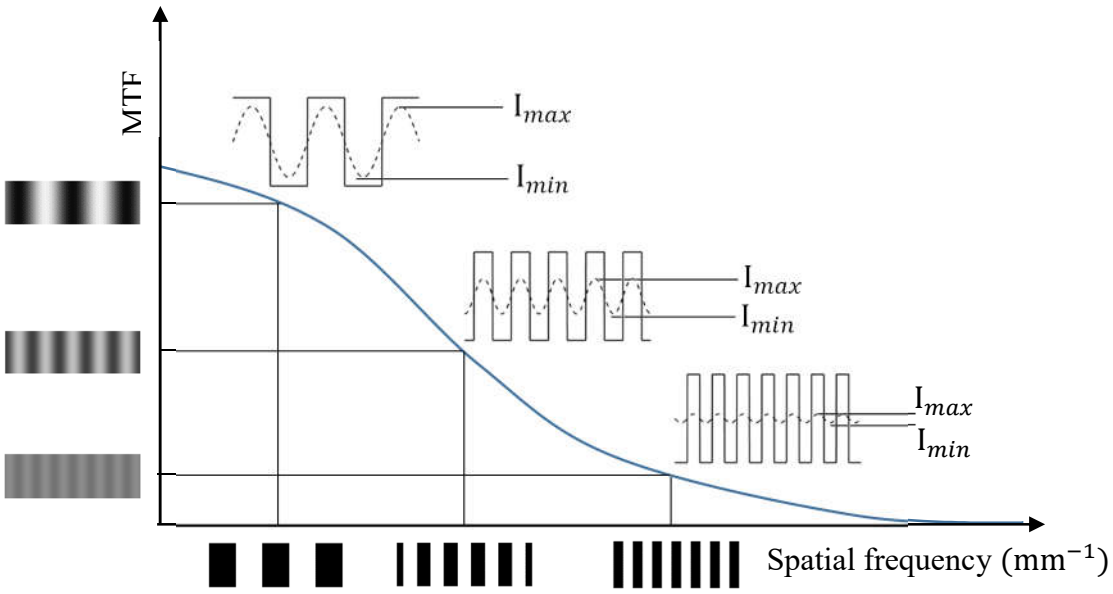

Figure 2.1 The MTF vs. contrast of the fringes at different spatial frequency

To sum up, we will model a projection system with astigmatic focus and shift the image plane to a different distance and observe the MTF. At each distance, the MTF value at the required frequency is the image contrast. Then repeat the same process for a different depth, we could find the relationship between the depth information and the contrast ratio.

2.3 Simulation Method

For the endoscopic application, both the projection lens and cylinder lens should have a small diameter. So, we use a GRIN lens as projection lens and a cylindrical lens with the small diameter

to provide astigmatism. The refractive index of a GRIN lens varies continuously as a function of spatial coordinates in the medium. There are some benefits to use GRIN lens. Firstly, GRIN lens can be manufactured very small, which is hard for the manufacture of the conventional lens. Secondly, the end of the GRIN lens surface could be flat which is convenient to couple with the optical fiber. Thirdly, GRIN lens could be used to reduce aberration. The limitation of GRIN lens is chromatic aberration. This problem can be neglected if we consider monochromatic illumination. The GRIN lens in the simulation is GT-IFRL-100-020-50-NC from GRIN TECH Gradient Index Optics Technology. Table 2.1 shows the parameters for this GRIN lens.

Table 2.1 GT-IFRL-100-020-50-NC parameters

Diameter	1.0 mm	Reflection index in the center	1.635
Working distance	20 mm	Designed wavelength	570 nm
Lens length	2.29 mm	Paraxial magnification	-23.1
NA	0.5		

The cylinder lens is Edmund # 47-760. It is the smallest off-of-the shelf cylinder lens; it is suitable for the prototype and simulation purpose. We optimize the lens separation in Zemax and insert an additional thin lens in between the GRIN lens and cylinder lens for better image quality. The off-the-shelf choice for this lens is bi-convex lens ROLYN OPTICS 110023. The parameters for the cylinder lens and the additional thin lens are shown in table 2.2

Table 2.2 Parameters of the cylinder lens and the additional thin lens

	Cylinder lens	Additional thin lens
	Edmund # 47-760	ROLYN OPTICS 110023
Diameter	5 mm	6.4 mm
Focal length	8 mm	16 mm
Center thickness	3 mm	1.1 mm

Figure 2.2 is the Zemax model of the projection system. We put the convex surface of the cylinder lens toward the incident light to reduce the spherical aberration. Figure 2.3 shows the spot diagram

for on-axis field and 0.1mm field through the central reference focus plane. In this simulation, the cylinder lens brings extra power in the vertical direction. The spot diagram shows that the rays focus on the vertical direction first then focus on the horizontal direction as the image plane moves further from the lens.

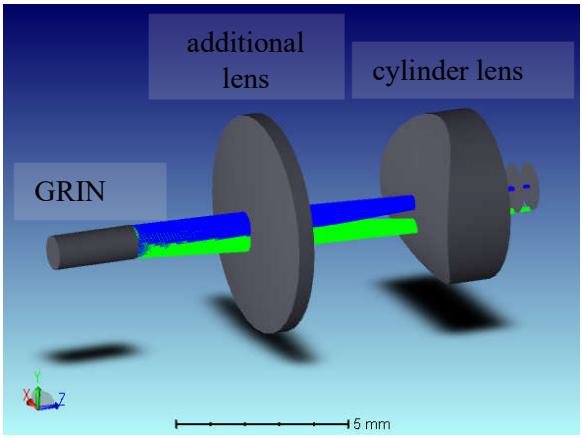

Figure 2.2 The Zemax model of projection system with cylinder lens

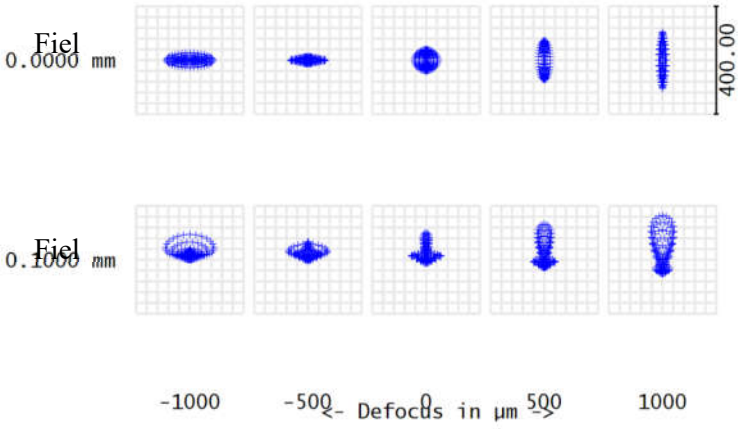

Figure 2.3 The spot diagram through the reference focal plane

2.4 Simulation Result

In this simulation, we observe the MTF result to find out the relationship of contrast ratio vs. depth. We will also talk about the influence of the pattern frequency and the field and the illumination wavelength.

For the same image plane, different pattern frequencies will lead to different MTF values which means different image contrast. Naturally, the pattern frequency will have an influence on the contrast ratio vs. depth relationship. The field is another factor because that astigmatism is an off-axis aberration that varies quadratically with image height in the wavefront form. From the diffraction theory of MTF calculation, we know that MTF is also based on the wavelength. So, the wavelength is another factor will impact the result.

Figure 2.4 is the MTF plot through the focus plane at different frequencies with wavelength 0.5876 μm. For each subplot, the MTF information includes the tangential and sagittal MTF for a different field. Figure 2.5 is the contrast ratio vs. depth for different frequencies.

From Figure 2.5 we can tell that the relationship between the contrast ratio and depth changed with the frequency in two fields. The simulation for the frequency at 3 cycles/mm and 5 cycles/mm is better than the high frequency because the result is monotonic. The monotonic range will determine the depth map range. If the contrast ratio is monotonic in a broad depth range, it means this model applies to measure a broad depth range. For the higher frequency result, the monotonic range is smaller, but the plot is steeper which means the depth measurement could be more accurate. There is a trade-off between the depth range and accuracy.

Figure 2.6 shows the contrast ratio vs. depth for different wavelengths. In this simulation, the frequency is 5 cycles/degree with the wavelength 587.6 nm, 656.3 nm, 486.1 nm as well as the polychromatic light (same weighting for 587.6 nm, 656.3 nm, 486.1 nm). From the result, we can tell that for the 587.6 nm, 656.3 nm, and polychromatic light the plot is monotonic. For the 587.6 nm and polychromatic light, the plot for different fields are close to each other. Hence the green light and the polychromatic light are the better option in the system.

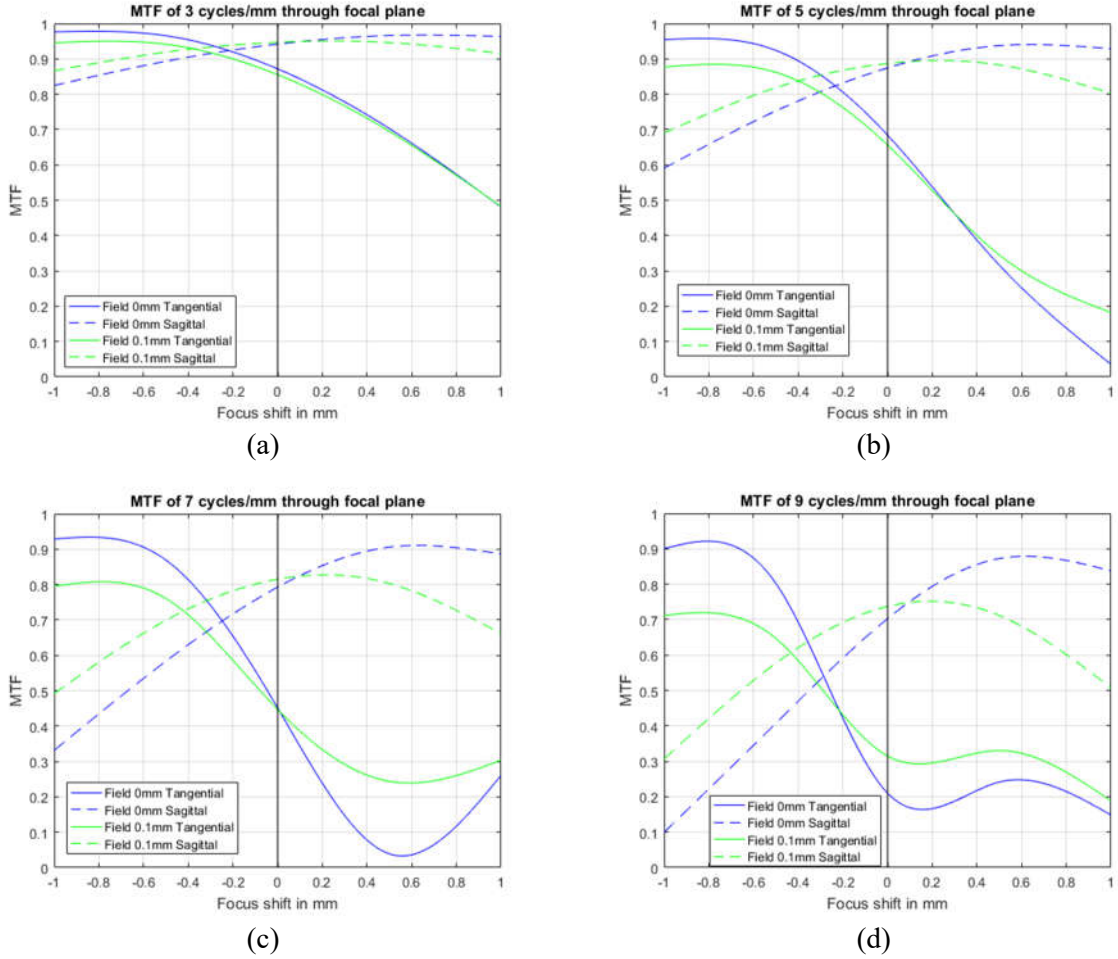

Figure 2.4 The MTF plot through the focus at different frequency with wavelength 0.5876 μm

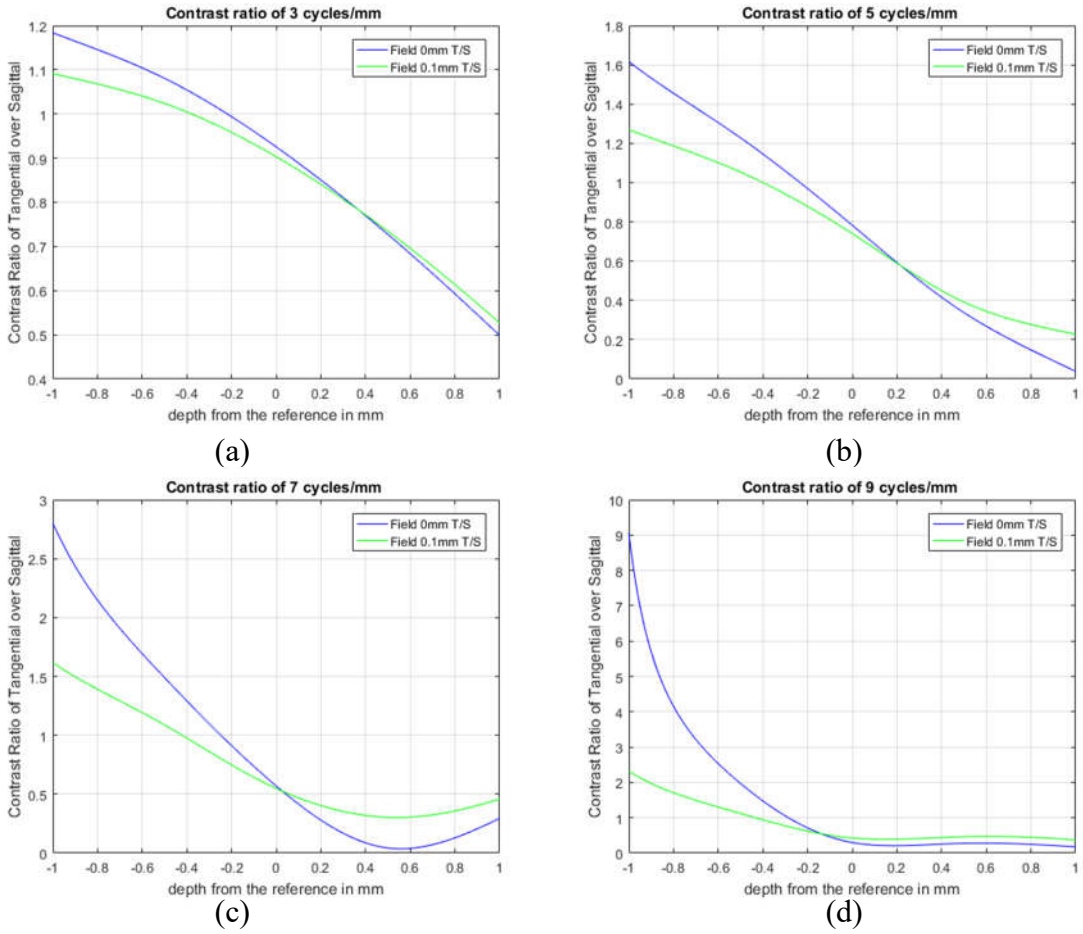

Figure 2.5 The contrast ratio vs. depth for different spatial frequency

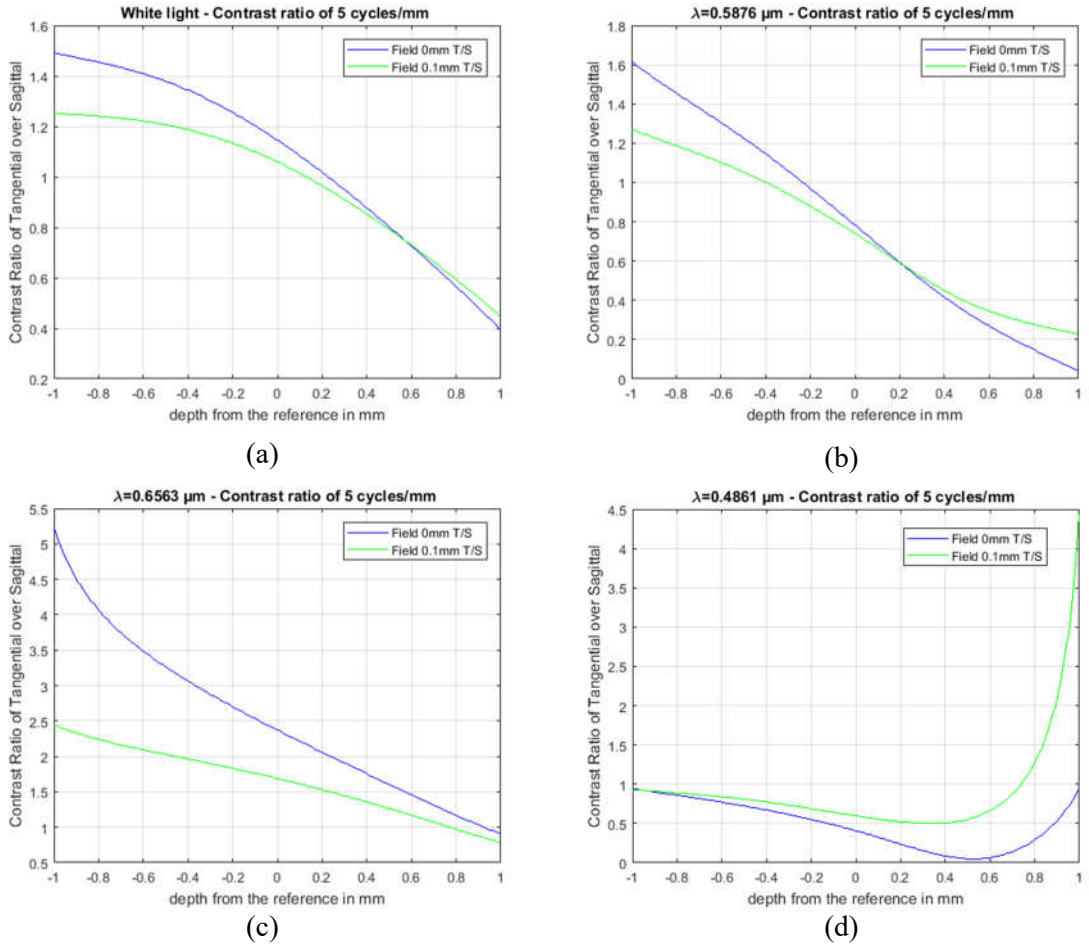

Figure 2.6 The contrast ratio vs. depth for different wavelength

2.5 Conclusion

In this chapter, we introduced the contrast measurement through the image MTF and built the Zemax model for a projection system with a cylinder lens in the endoscopic size. The simulation result shows that the controlled aberration method can be implemented in the endoscopic scale. At the same time, the pattern frequency and test field and wavelength all influent the relationship of the contrast ratio vs. depth. Those results will help us in choosing the projection pattern frequency as well as achieve accurate calibration by considering the field. At last, considering the influence of different wavelength, the experiment should be operated with a green light or polychromatic light.

CHAPTER 3

PROTOTYPE DESIGN AND SET-UP

3.1 Introduction

This chapter is about the design details of the controlled aberration 3D endoscopic prototype. In this chapter, section 3.2 is about the overall system design of the controlled aberration 3D endoscopic prototype. This prototype includes an illumination path (projection path) with astigmatism and an imaging path. Section 3.3 is about the illumination path design. This projection path is the critical part of the prototype. It includes four parts: a light source; coupling lens; relay system and the projection system with astigmatism. Section 3.4 is about the imaging path.

3.2 Overall System Design

The controlled aberration method is a uniaxial depth measurement approach. Ideally, the illumination path and imaging path are coaxial in prototype. For simplicity, in this prototype, we put the imaging path close to the projection path. Figure 3.1 is the structure of this controlled aberration 3D endoscopic prototype. The illumination path projects the aberrated pattern onto the test scene. It includes the light source, coupling lens, an optical fiber relay and the projection optics with astigmatism.

The coupling lens forms an intermediate image of the pattern at the tip of the optical fiber; then the optical fiber carries this intermediate image to the other end of the fiber. Then this intermediate image is projected through the focusing optics and cylinder lens.

The imaging path could be a conventional 2D endoscope imaging path. The illumination path design is the primary work here. In this sense, the following sections will focus on the illumination path design.

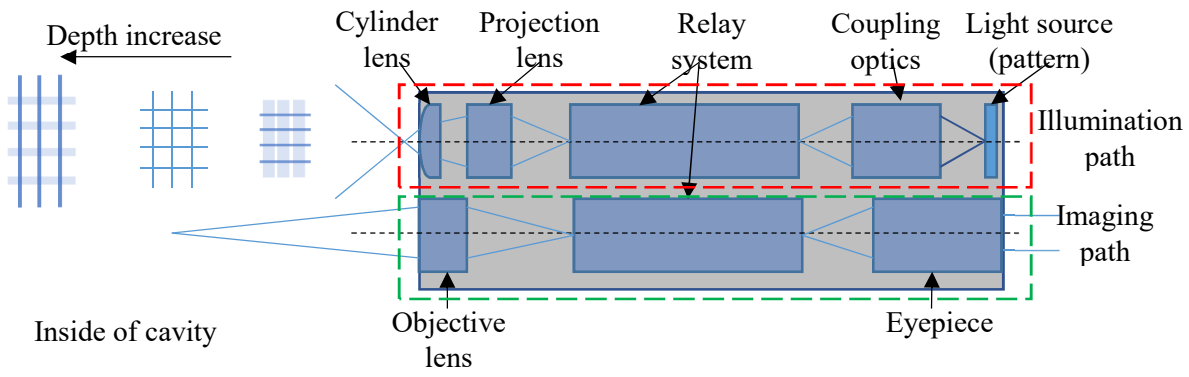

Figure 3.1 Endoscope with the aberrated projected pattern. The horizontal and vertical lines of the grid are in focus at different depths

3.3 Illumination Path Design

3.3.1 Light Source and Pattern Generator

The light source in this prototype needs to be used for illumination and the pattern generation at the same time. In this sense, we applied two approaches; one is the OLED miniature display, another is the DMD microchips with the LED light source.

3.3.1.1 OLED Light Source

OLED stands for the organic light emitting diodes. It is a flat light emitting device. There are two primary applications for OLEDs. One application is display, such as television screens, monitor screen; another application is illumination, OLED could offer diffuse area lighting. The OLEDs could be both the light source and the pattern at the same time. So,it is a reasonable option for the light source in this prototype.

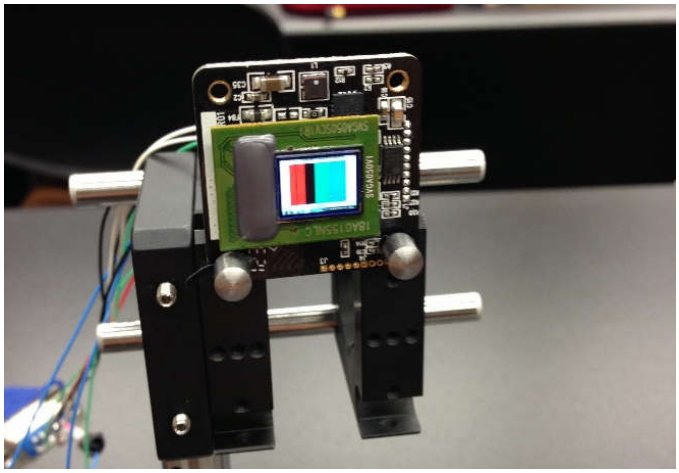

Figure 3.2 OLED SVGA050SC

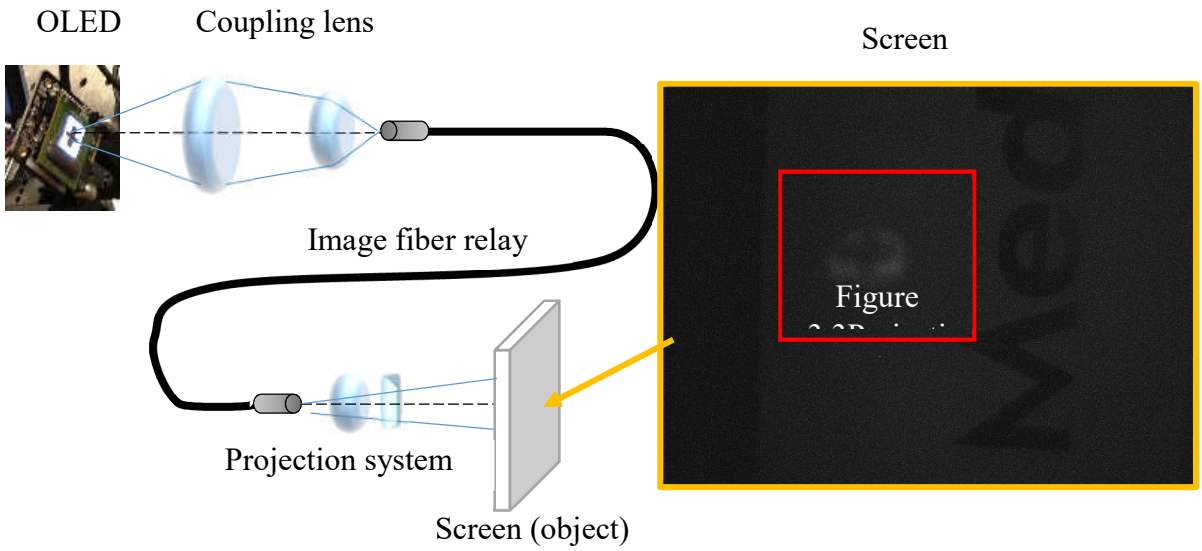

Figure 3.3 Projection path with OLED light source

Figure 3.2 is the OLED light source in this prototype. It is SVGA050SC from Yunnan North OLiGHTEK Opto-Electronic Technology Co., LTD. This device is Si-Base AMOLED Micro-display. The resolution is 800×600 (SVGA). The display area is 10.13mm×7.61mm (0.5 inches); The pixel pitch is 12.6 μm. It accepted 8/16/24 Bit Digital Video and YCbCr/RGB Color or Monochromatic input. The typical luminance is more than 70 cd/m^2.

Figure 3.3 is the scheme of projection path with the OLED light source. The image on the screen is too dim for depth measurement. So, we changed the light source to LED for illumination and used DMD chip to generate the pattern. The possible reasons include the low luminance of the OLED panel and the low coupling ratio due to the diffuse output light of the OLED.

3.3.1.2 LED Light Source and DMD Pattern Generator

The OLED is not bright enough to work as the light source in this application. To increase the light intensity while keeping the ability to project patterns, we choose LED as the light source and the DMD chips to generate the projection pattern.

LED stands for light-emitting diode. LED lights are energy efficient. It could be very bright and can be extremely compact. Due to those properties, LEDs are commonly used in the Pico projector as its light source.

DMD represents digital micromirror device.[33] It is a micro-opto-electromechanical system that is the core of the DLP (Digital Light Processing) projection technology from Texas Instruments (TI). A DMD chip has thousands of micro-mirrors arranged on its surface. Each of the micro-mirror corresponds to one pixel of the image to be displayed. Those micro-mirrors can be rotated $\pm 12°$. The positive state is micro-mirror titled toward the illumination, and it refers to the 'on' state. For a micro-mirror in the 'on' state, the corresponding pixel appears bright on the screen. The negative state is micro-mirror titled away from the illumination, and it refers to the 'off' state, making the pixel appear dark. Figure 3.4 [33] shows two pixels, one in the 'on' state and one in the 'off' state. Those are the only operational states of the micromirror. When we use it to produce greyscales, the mirror is toggled on and off quickly, and the ratio of 'on' time to 'off' time determines the shade produced. Contemporary DMD chips can produce up to 1024 shades of gray (10 bits).

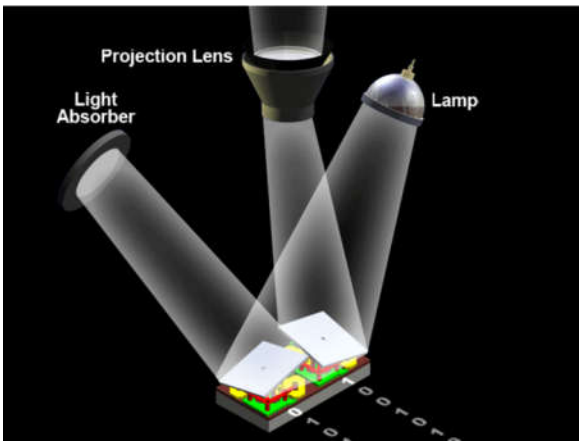

Figure 3.4. Micromirror in on and off mode. From "Introduction to ±12 Degree Orthogonal Digital Micromirror Devices (DMDs)," by Benjamin Lee, 2008 (http://www.ti.com/lit/an/dlpa008b/dlpa008b.pdf). Copyright [2008–2018], by Texas Instruments Incorporated. Reprinted with permission

The LightCrafter DLP Development Module from Texas Instruments is a projector based on the DMD. As shown in Figure 3.5 [34], it includes a DLP 0.3 WVGA chipset; an RGB LED light engine; a DMD controller board and a processor and interface board. For simplicity, we can use this DLP as the light source of controlled aberration endoscopic system by removing the projection optics in the light engine.

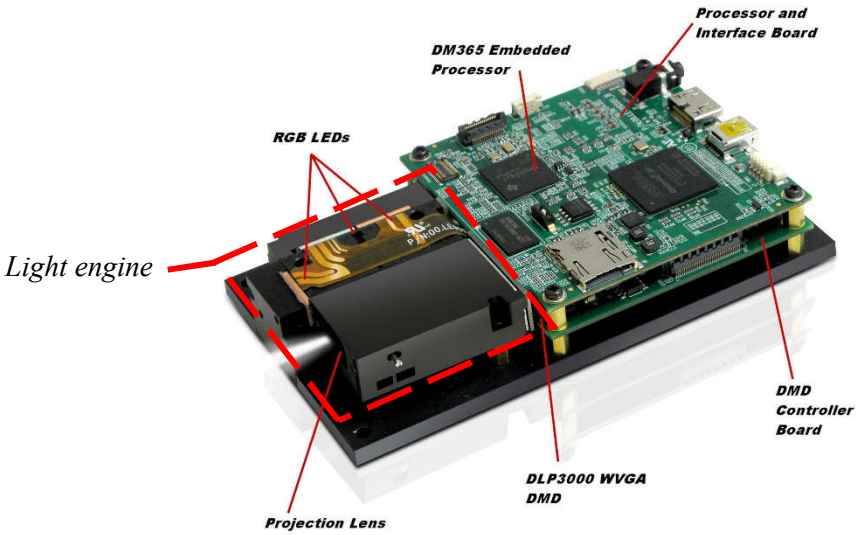

Figure 3.5 From "DLP® LightCrafter™ Evaluation Module" (http://www.ti.com/tool/DLPLIGHTCRAFTER). Copyright [1995–2017], by Texas Instruments Incorporated. Reprinted with permission

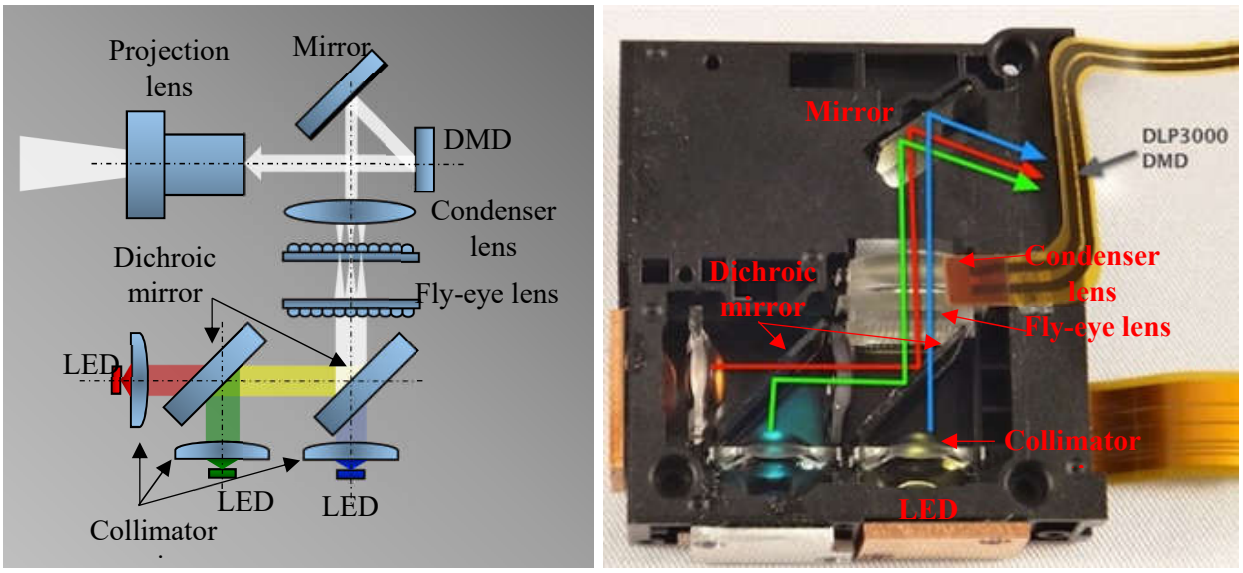

Figure 3.6 LightCrafter DLP Development Module light engine system layout. Right figure from "A look inside the Young Optics' Light Engine in LightCrafter" (https://e2e.ti.com/support/dlp__mems_micro-electro-mechanical_systems/advanced_light_control/f/850/t/162664). Copyright [1995–2017], by Texas Instruments Incorporated. Reprinted with permission

Table 3.1 The parameters of light engine

RGB LED	20 lumens output	Nyquist frequency	65 lp/mm
DLP3000 DMD resolution	608 * 684	Cover window glass refractive index	1.5078
Diagonal micromirror array	7.62 mm	Window transmission	97%
Micromirror pitch	7.6 um	Window reflectivity	88%

Table 3.1 is the parameters of the light engine. Figure 3.6 is the light engine system layout. There are three LED light sources with R, G, B color. Each LED has a collimating lens to create the collimated beam. This collimated light beam passes through a set of dichroic mirrors which only reflect a narrow band of the light wavelength while letting the light with other wavelengths pass

through it. The dichroic mirrors recombine the R, G, B light beams into one co-linear white light beam. The recombined light passes through a pair of fly-eye lenses and a condenser lens that provides uniform light intensity. Then the uniform light beam is reflected by a mirror towards the DMD chip. By controlling the micromirrors on the DMD chip, the output beam will project the target image through the projection optics onto the screen. In this prototype, we use this light engine as the light source by removing the projection lens.

3.3.2 Coupling Optics

The coupling optics focus the output light from DMD into the optical fiber relay. For this coupling optics, the object is the DMD chip, and the image locates at the image fiber surface. Both DMD size and the image fiber size are fixed. To keep the magnification unchanged, we choose a double telecentric lens as the coupling optics.

A double-telecentric lens is a compound lens that has its entrance and exit pupil at infinity. Figure 3.7 is a most straightforward double-telecentric afocal system. The chief ray is parallel to the axis in object space and image space. Since the ray bundle is centered on the chief ray, the magnification is independent of the axial object's shift or image plane shift. Telecentric lens could eliminate the perspective error because chief ray is parallel to the optical axis. High-quality telecentric lenses also show a low distortion degree, in the range of 0.1%.

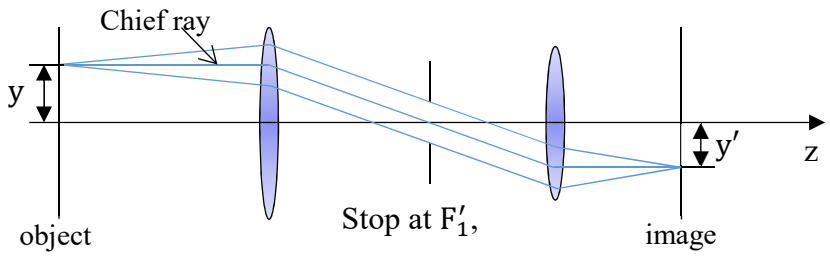

Figure 3.7 Layout of a double telecentric system

The coupling lens creates an intermediate image of the DMD pattern on the tip relay optics. In this prototype, we choose image fiber as the relay system. The typical image fiber channel diameter in the commercial flexible endoscopes is around 1mm to 3mm. The diagonal of DMD chip is 7.62mm. In this sense, the magnification of this telecentric system should be around 0.14 to 0.3937. So, we choose the Bi-telecentric lens TC2348 from Opto-engineering company with magnification of 0.184. Figure 3.8 is the black box plot of this bi-telecentric lens TC2348. Table 3.2 gives the first order parameter of this system. Figure 3.9 is the MTF of the bi-telecentric lens TC2348. Figure 3.10 is the distortion and field curvature of this system. Both figure 3.9 and figure 3.10 are reprinted based on the zemax file of TC2348 provided by Opto-engineering company.

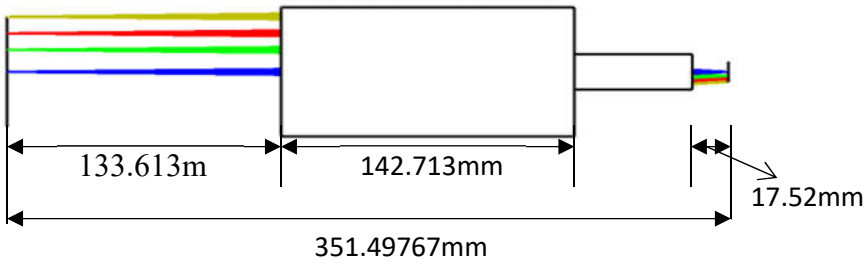

Figure 3.8 Layout of the black box plot of the bi-telecentric lens TC2348 (Courtesy Opto-engineering company)

Table 3.2 System/Prescription Data of Bi-telecentric lens TC 2348 (in mm)

Effective Focal Length	2561.94	Object Space NA	0.01149
Back Focal Length	-252.91	Paraxial Image Height	5.51
Total Track	217.89	Paraxial Magnification	-0.18
Image Space F/#	4.20	Entrance Pupil Diameter	610.56
Paraxial Working F/#	8	Entrance Pupil Position	26443.04
Working F/#	8.00	Exit Pupil Diameter	123.75
Image Space NA	0.06	Exit Pupil Position	-990.18

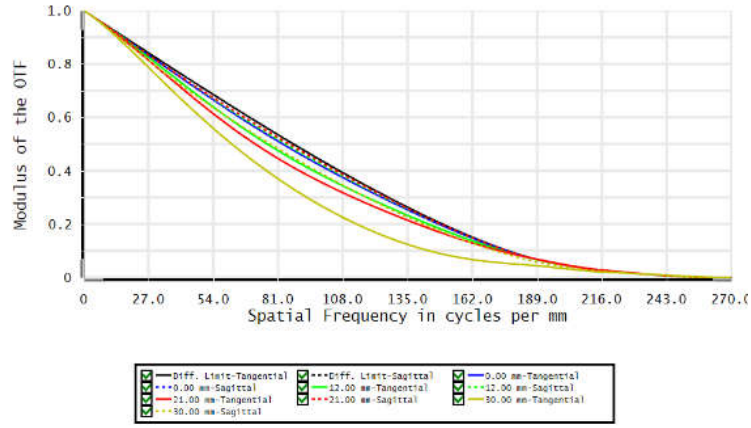

Figure 3.9 The MTF of Bi telecentric lens TC2348 (Courtesy Opto-engineering company)

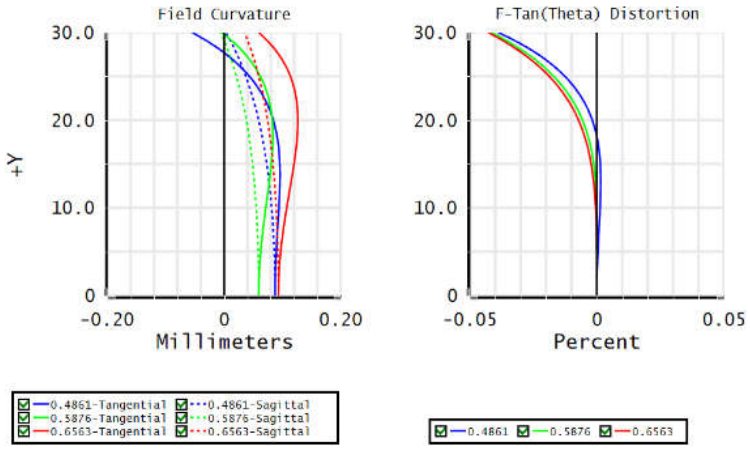

Figure 3.10 Field Curvature and distortion of the bi-telecentric system (Courtesy Opto-engineering company)

3.3.3 Image Fiber Relay System

The telecentric lens creates the first intermediate image of the pattern. To extend the optical path and bring the intermediate image into the distal of the endoscope, we need relay lens here. In the rigid endoscope configuration, conventional relay system or rod lens or GRIN lens could work as the relay system. In the flexible endoscope, people use optical fiber as the relay system. In this prototype, we choose the image fiber relay for simplicity.

An optical fiber is a flexible, transparent filament made of the light guiding dielectric material such as plastics and glasses. It is a waveguide that transmits light between the two ends of the fiber by total internal reflection. An optical fiber consists of three sections. The center of the structure is called the core. The inner core is made of high refractive-index material. Most of the optical energy is confined to this area. The core is surrounded by the low refractive-index material called the clad. Total internal reflection will confine the light rays entering the core within the critical angle at the core-clad interface. The clad is usually covered by additional layers of protective material. These additional layers do not have a direct role in light confinement.

Most light-delivery bundles contain unaligned optical fibers and are used only to transmit energy. In contrast, imaging fibers are bundles in which the position of each optical fiber is the same as the input and output ends. Image fiber is also called a coherent bundle of fibers. In these bundles, each optical fiber acts as a pixel, and the size of the pixel determines the resolution of the transmitted image. In the conventional fiberscope, people use the incoherent optical fiber for illumination and image fiber for imaging.

In this application, the illumination path also needs to project a pattern on the target scene. So, we use the image fiber as a relay system in this projection path. It brings the first intermediate image formed by the bi-telecentric lens into the distal of the endoscope to create the second intermediate image. The second intermediate image works as an object for the projection lens. From section 3.3.1 and section 3.3.2, we know the diagonal of DMD chip is 7.62mm, the magnification of the bi-telecentric lens is 0.184. So, the diagonal of intermediate image size is 1.402mm. In this application, we choose FIGH-30-850N image fiber with 1mm diameter and 30000+3000 pixels.

3.3.4 Projection Optics with Cylinder lens

The design of this part is mainly introduced in Chapter 2. We use a GRIN lens GT-IFRL-100-020-50-NC as the projection lens. This GRIN lens is directly glued to the image fiber tip. The cylinder lens is Edmund # 47-760. The cylinder lens locates at the end of the projection path to add astigmatism to the projection. To improve the image quality, an additional thin lens ROLYN OPTICS 110023 can be inserted in between the GRIN lens and cylinder lens. This additional lens

is not mandatory, a prototype still works without it. Figure 2.2 shows the configuration of the projection lens and cylinder lens.

The cylinder lens has power in one direction. Its equivalent to a parallel plate in one direction, and it works as a plano-convex lens in another direction. In this design, the curved surface is towards to the source to reduce the spherical aberration. The reason is if the plane surface is toward to the source, all the refraction happened at the convex surface, if the curved surface is toward to the source, the overall refraction of each ray is distributed on both surfaces. Figure 3.11 is the projection on a screen with the checkboard pattern through GRIN lens and a cylinder lens.

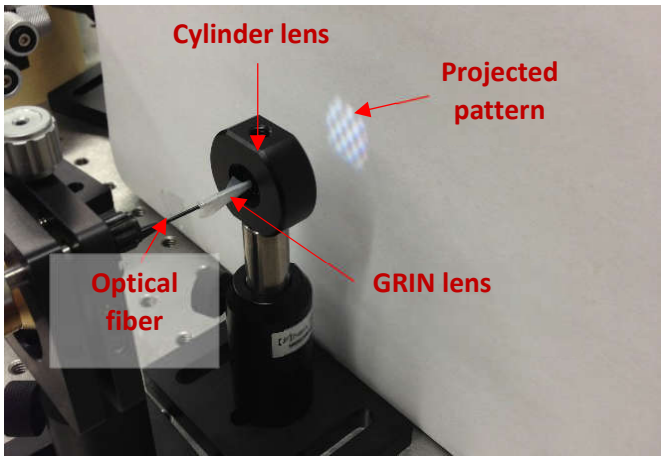

Figure 3.11 Projection on a screen with checkboard pattern via the GRIN lens and cylinder lens

3.3.5 Overall Illumination Path

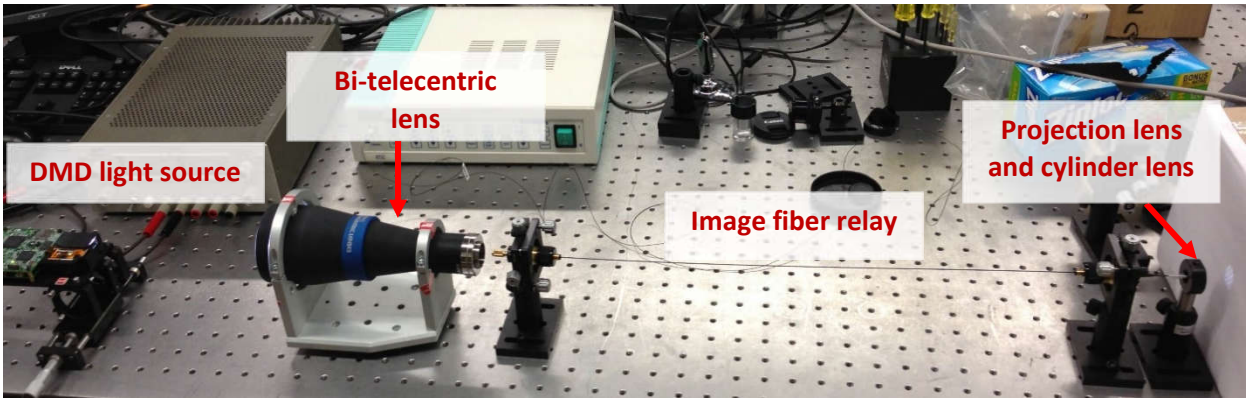

Figure 3.12 Prototype of the illumination path

Figure 3.12 shows the prototype of the illumination path for the controlled aberration 3D endoscope. The LED light source emits light onto the DMD chips. The DMD chip is coded with the projection pattern, and the output light will be focused to form an intermediate image by the bi-telecentric lens. Then place the image fiber on this intermediate image and bring this intermediate image to another end of the image fiber. Then this second intermediate image will be projected through a GRIN lens and cylinder lens onto the test scene.

3.4 Imaging Path Design

The imaging path in this prototype could be the same as the image path in the conventional 2D endoscope. It is constructed by an objective lens, a relay system and imaging optics for sensor or eyepiece for human observation. As we introduced in chapter 1, the relay system could be conventional relay system or lens rods or GRIN lens through the rigid endoscope or coherent fiber bundle in the flexible endoscope.

The controlled aberration depth measurement method works in the uniaxial configuration, hence there is no separation required between the illumination path and the image path. Theoretically, the relay system in the illumination path and the image path play the same role. In this sense, there

is potential to use the same relay system for both illumination path and imaging path to further reduce the diameter of the endoscope.

In this prototype, the cylinder lens is at the end the illumination path. To simplify the system and keep the separation between two paths as small as possible. We firstly used the mini camera to form images. This mini camera has 1.2mm diameter, and it is waterproof. However, this mini camera suffers from low resolution and high distortion. To overcome those problems, the second configuration for depth measurement is using the DSLR camera on-axis for the transmittance image.

3.4.1 Mini Camera

The mini camera in this prototype is Medigus 1.2 mm diameter CMOS camera. It integrates five pieces focusing lens and a miniature CMOS sensor in 5mm length with 1.2mm outer diameter. Table 3.3 gives its specification. Due to the compact size, it is an excellent option to be imaging path in this prototype.

Table 3.3 Micro ScoutCam™ 1.2mm specifications

Outer diameter	1.2mm	Cable length	2m
Length	5mm	Frame rate	30fps
Sensor resolution	49,280px	Field of view	100°
Pixel size	2.2µm X 2.2µm	Depth of field	2-6mm
Image area	492.8µm x 488.4µm	Sensor type	CMOS
Cable diameter	0.58mm	Scan mode	Progressive
Working distance	10mm	Color mosaic	RGB Bayer pattern

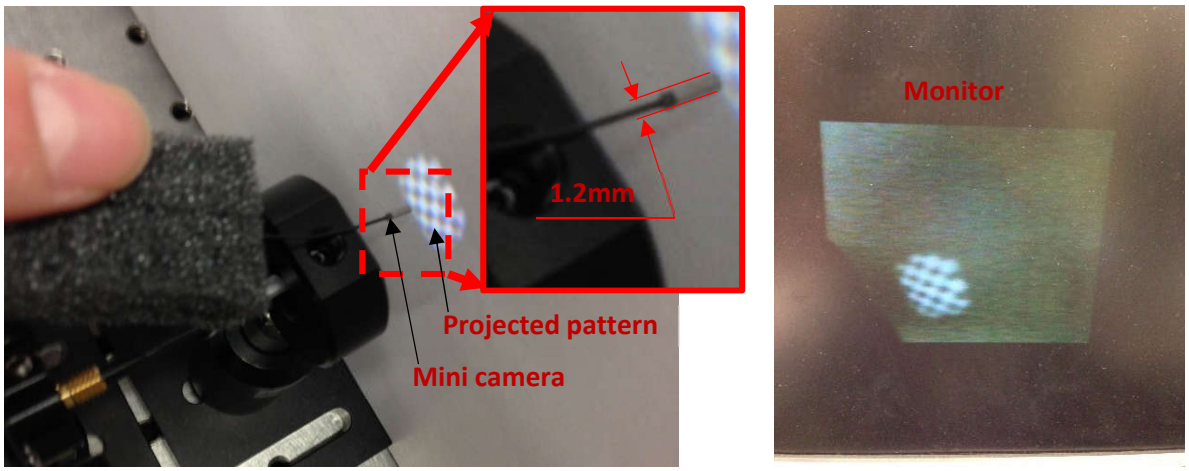

Figure 3.13 (a) is mini camera (b) is the image captured by the mini camera

Figure 3.13 (a) shows we use the mini camera to capture a projected pattern. (b) shows the pattern image captured by the mini camera. This mini camera has a perfect size for the endoscope application. However, the image captured by this mini camera has significant distortion, and the resolution is low.

Due to those problems, we implemented another configuration with DSLR camera. We placed the DSLR camera on axis after a diffuser screen, so there is no separation between the illumination path and imaging path. It captures the transmitted image of the aberrated pattern on the diffuser screen and presents the depth measurement based on this image. Details will be discussed in chapter 4.

3.5 Conclusion

In this chapter, I talked about the prototype design of the controlled aberration 3D endoscope. This prototype is constructed with the illumination path and imaging path.

In the illumination path, we showed the choices for the light source, a coupling lens, relay system and a projection lens. There are two light source configurations, one is OLED, and another is LED

with DMD chip. The LED with DMD configuration is better because it is brighter than OLED. The coupling lens is a bi-telecentric lens for constant magnification. The relay system is a coherent optical fiber bundle for simplify and small diameter. The projection system is a GRIN lens with a cylinder lens.

The benefit of the controlled aberration depth measurement is there is no separation required for illumination path and imaging path. For the imaging path, we showed the configuration with the miniature camera for the reflected pattern image. The diameter of this mini camera is 1.2mm. It was placed close to the illumination path. However, the miniature camera suffered the low resolution and high distortion. The second configuration is DSLR on axis to capture the transmitted image to overcome those problems.

CHAPTER 4

EXPERIMENTS

4.1 Introduction

This chapter is focus on the depth measurement experiments. The first experiment is based on the miniature camera locates at the same side as the projection path. The miniature camera had a small diameter and was placed right next to the projection path. This configuration can be treated as uniaxial. The problem is this miniature camera has low resolution and high distortion. So, it is hard to achieve an accurate calibration. Furthermore, it is hard to implement an accurate depth measurement. So, in the miniature camera experiment, we only measure the pattern image contrast ratio of a step object. If there is a noticeable difference between the contrast ratio for different depths, it means there is potential to measure the depth information based on the controlled aberration method for the endoscopic application.

The alternative configuration is a miniature camera with high resolution and better image quality. However, the current commercial products cannot fulfill this requirement. For simplicity, we use a DSLR camera behind the diffuser screen to capture the transmitted image. In this configuration, the aberrated pattern is projected onto diffuser screen. The screen acts as the "detector," and the DSLR camera only captures the screen for the image. This configuration is not applicable for the actual endoscope. We only use this configuration to prove the depth measurement ability. In the practical endoscope design, the imaging path should be on the same side of the illumination path to capture the reflected image of the test scene with aberrated projection pattern.

In this chapter, section 4.2 is the experiment with the miniature camera. It includes the experiment setup and contrast calculation algorithm, as well as the result analysis. Section 4.3 is the experiment with the on-axis diffuser and DSLR camera. It includes the calibration process and the depth measurement with two separated diffuser screens.

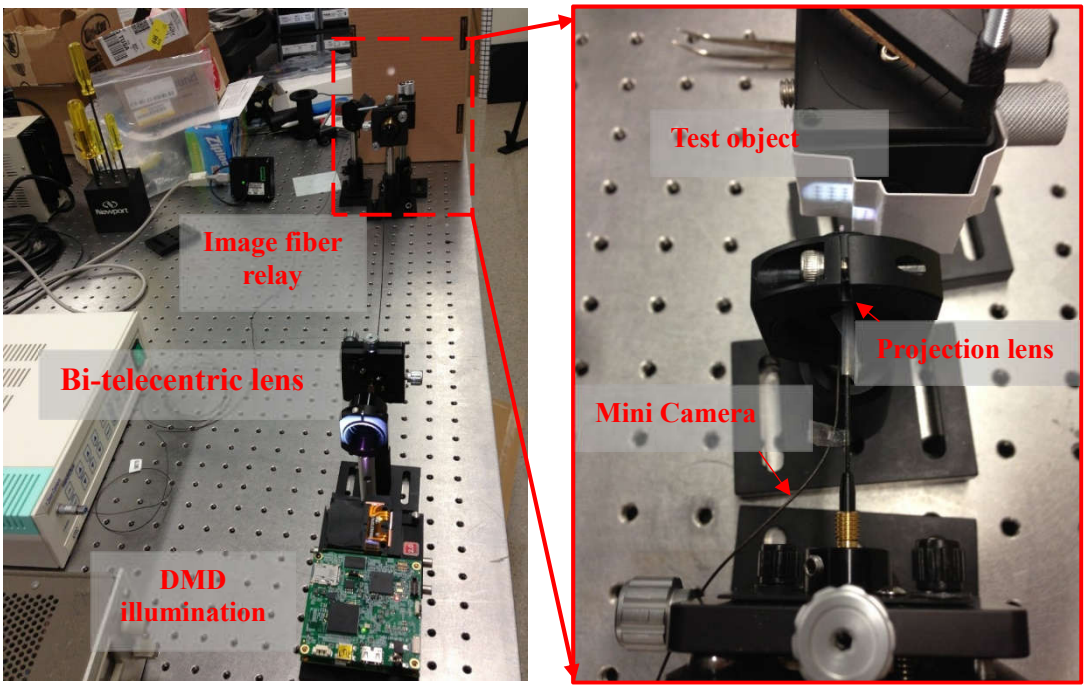

Figure 4.1 Setup for the experiment with miniature camera

4.2 Experiment with miniature camera

Figure 4.1 shows the setup for the experiment for the mini camera. The mini camera is placed close to the projection path. Since both the projection path and mini camera have a small size, we can still consider that there is no separation between the illumination path and imaging path. The mini camera has a 224×220 resolution. It is much lower than the stereo endoscope Da Vinci system which has a 1920×1080 resolution. A test object is an object with step shape, the height of its left side and the right side is different. The projection pattern is multiple crosses as designed by G. Birch. [32] In the completed system, the projected pattern need to be switched on and off for the pattern image of the scene and the background image of the test scene. The background image keeps the high spatial resolution as the conventional 2D endoscope, and the switching of the projected pattern will eventually determine the time resolution of the system.

4.2.1 Algorithm for Contrast Calculation

In the measurement, we capture two images for each scene. One is the image with the pattern, and the other is the background image without the crosses pattern. This background image is required to deal with the intensity non-uniformity through the Field. In this section, we introduce the contrast calculation and image segmentation algorithm. The contrast calculation is based on the Haar wavelet coefficients, and the image segmentation is based on the watershed algorithm. Figure 4.2 illustrates the whole process.

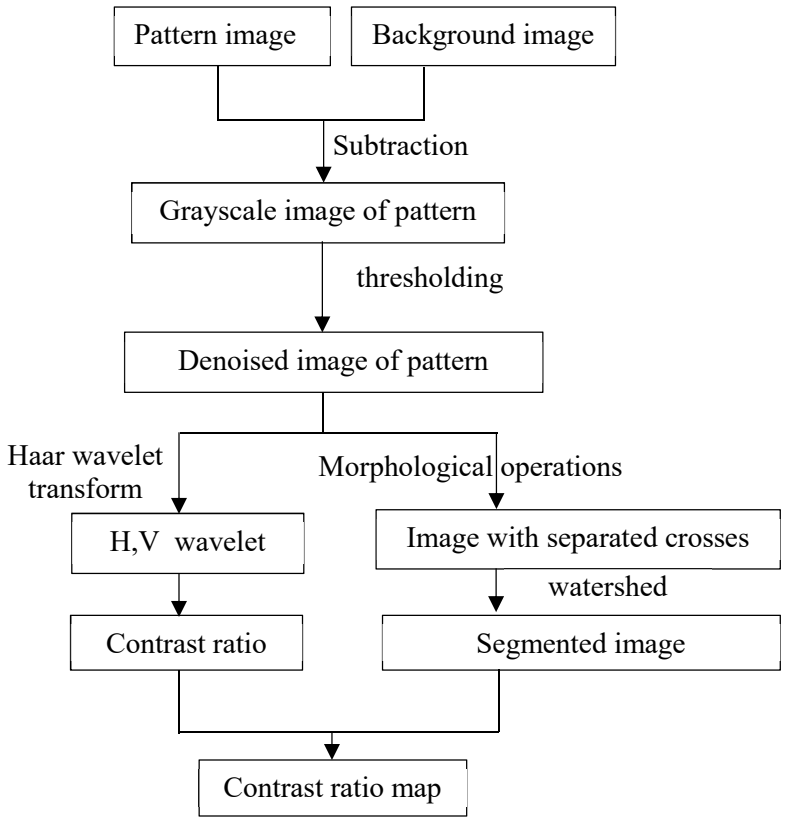

Figure 4.2 Algorithm flow for the contrast ratio map

We capture two images for each test scene. One image is this object illuminated with the pattern (Figure 4.3 left), and another one is the test object illumination with backlight (Figure 4.3 middle). By subtracting the background image from the pattern image for one color channel, we can get the grayscale image of the pattern (Figure 4.3 right). Then we use morphological operation to denoise

and separate the connection of the cross pattern. For this cleaned image pattern, we use the watershed algorithm for image segmentation to find the area for each cross, then use Haar wavelet algorithm to calculate the contrast ratio for the corresponding cross area. At last, plot the contrast ratio map.

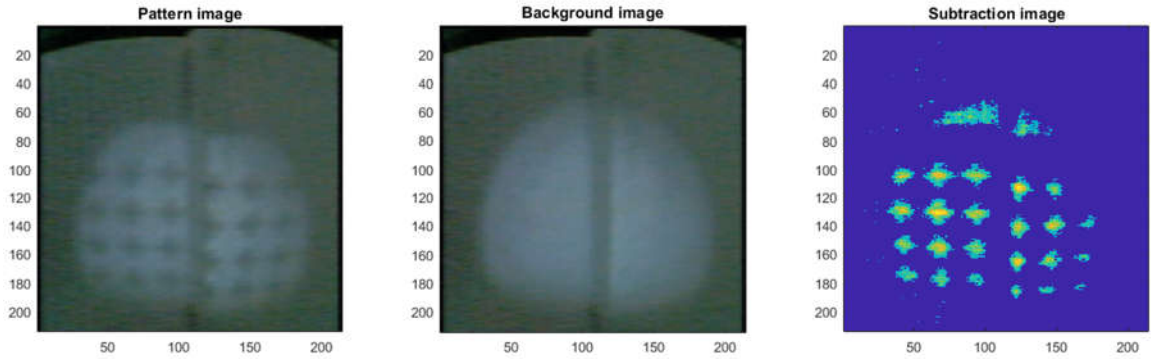

Figure 4.3 Pattern image (left) Background image(middle) Subtraction image (right)

4.2.2 Contrast Calculation in the Wavelet Domain

The contrast of an image can be calculated by the Michelson's contrast equation for the periodical signal and with the maximum intensity I_{max} and the minimum intensity I_{min} as

$$\text{Contrast} = \frac{I_{max} - I_{min}}{I_{max} + I_{min}} \tag{4.1}$$

The Michelson contrast can also be calculated in the wavelet domain. [35-39] As we know from the Fourier theory, the signal can be expressed as a sum of a series of sinusoidal signals, but it lacks the location information. The wavelet transform can provide the space and frequency information simultaneously. In another word, with the wavelet transform, we can get the frequency components of an image also the location they are presenting. The wavelets are localized wavelike functions[40] which are being matched to the particular structure of the image. Mathematically, the wavelet transform can be interpreted as the convolution of the signal with a wavelet function. The wavelet transform implements the multi-resolution decomposition of an image.[41] The

general method of the multiresolution decomposition is to generate an approximation component using a scaling function (low-pass filter) and the detail component using a wavelet function (high-pass filter). [40] Based on the idea of multi-resolution decomposition, we can use the wavelet transform in the multi-scale local contrast measurement. [37]

The following part is about the local contrast calculation method for 2D image f(x, y) in the wavelet domain. [42] The 2D scaling function can be defined as $\Phi(x, y)$, the wavelets along the horizontal, vertical and diagonal directions are $\Psi^{h}(x,y), \Psi^{v}(x,y), \Psi^{d}(x,y)$ respectively. The wavelets work as the high-pass filter and extract the edges for the corresponding directions. For the level j wavelet transform, the scale factor is 2^{j} and the corresponding basis wavelets becomes into

$$\Phi_{j,m,n}(x, y) = 2^{j}\Phi\left(2^{j}x - m, 2^{j}x - n\right) \quad (4.1\ a)$$

$$\Psi_{j,m,n}(x, y) = 2^{j}\Psi\left(2^{j}x - m, 2^{j}x - n\right) \quad (4.1\ b)$$

(m,n) are the location in the subspace. The wavelet coefficients for level j wavelet transform of the image are:

$$a_{j,m,n}(x, y) =< f(x,y), \quad \Phi_{j,m,n}(x,y) > \quad (4.2\ a)$$

$$h_{j,m,n}(x, y) =< f(x,y), \quad \Psi^{h}_{j,m,n}(x,y) > \quad (4.2\ b)$$

$$v_{j,m,n}(x, y) =< f(x,y), \quad \Psi^{v}_{j,m,n}(x,y) > \quad (4.2\ c)$$

$$d_{j,m,n}(x, y) =< f(x,y), \quad \Psi^{d}_{j,m,n}(x,y) > \quad (4.2\ d)$$

In the equation, <> indicate the inner product. As a result, the image f(x, y) can be presented as the orthogonal wavelet with J levels.

$$f(x,y) \sim [A_j, (D_j^H, D_j^V, D_j^D), \quad j \in (J, J-1, \dots, 1)] \quad (4.3)$$

Where $A_J = \{a_{J,m,n}; m,n \in Z\}$, $D_J^H = \{h_{J,m,n}; m,n \in Z\}$, $D_J^V = \{v_{J,m,n}; m,n \in Z\}$, $D_J^D = \{d_{J,m,n}; m,n \in Z\}$. Those are the decomposition of the original signal into sub-band signals with

different frequency content. local contrast of this resolution (frequency) corresponding to level j at different directions are

$$\begin{aligned} Horizontal\ contrast \quad & C_j^H = \frac{D_j^H}{A_j} \\ Vertical\ contrast \quad & C_j^V = \frac{D_j^V}{A_j} \\ Diagonal\ contrast \quad & C_j^D = \frac{D_j^D}{A_j} \end{aligned} \tag{4.4}$$

In this application, we need to calculate the contrast ratio of horizontal and vertical direction. This contrast ratio can be written as

$$\mathrm{R_j} = \frac{\frac{D_j^H}{A_j}}{\frac{D_j^V}{A_j}} = \frac{D_j^H}{D_j^V} \tag{4.5}$$

So, by decomposing the image of the pattern at required resolution and dividing the coefficients of horizontal wavelet by vertical wavelet coefficients, we can get the contrast ratio value for each pattern area on the captured image.

The following part is an example of the Haar wavelet transform in the contrast calculation. Haar wavelet is the simplest type of the discrete wavelet. As all wavelet transforms, the Haar transform decomposes a discrete signal into two sub-signals of half its length. One sub signal is a running average or trend (low-pass filtered); the other sub-signal is a running difference (high -pass filtered). Take level-1 Haar wavelet for example, the wavelets are defined as:

$$\begin{aligned}
\Psi_{1,1} &= (\frac{1}{\sqrt{2}}, \frac{-1}{\sqrt{2}}, 0,0, \dots, 0) \\
\Psi_{1,2} &= (0,0, \frac{1}{\sqrt{2}}, \frac{-1}{\sqrt{2}}, \dots, 0) \\
&\vdots \\
\Psi_{1,N/2} &= (0,0, \dots, \frac{1}{\sqrt{2}}, \frac{-1}{\sqrt{2}})
\end{aligned} \tag{4.6}$$

The subscript 1,2,…N/2 indicate the location information, the subscript 1 means the level 1. The edge information $d_{1,m}$ for a signal f with N elements based on the level-1 Haar wavelets is the scalar product of the signal and the wavelets

$$d_{1,m} = \mathrm{f} \cdot \Psi_{1,m} \qquad m = 1,2, \dots, N/2 \tag{4.7}$$

The scaling functions (low-pass filter) are represented as:

$$\begin{aligned}
\Phi_{1,1} &= (\frac{1}{\sqrt{2}}, \frac{1}{\sqrt{2}}, 0,0, \dots, 0) \\
\Phi_{1,2} &= (0,0, \frac{1}{\sqrt{2}}, \frac{1}{\sqrt{2}}, \dots, 0) \\
&\vdots \\
\Phi_{1,N/2} &= (0,0, \dots, \frac{1}{\sqrt{2}}, \frac{1}{\sqrt{2}})
\end{aligned} \tag{4.8}$$

So, the low-frequency components of the signal f at different location m can be expressed as

$$\mathrm{a}_{1,m} = \mathrm{f} \cdot \Phi_{1,m} \qquad m = 1,2, \dots, N/2 \tag{4.9}$$

Similarly, for the level-2 Haar wavelet, the wavelets are defined as Ψ_{m}^{2}

$$\begin{aligned}
\Psi_{2,1} &= (\frac{1}{2},\frac{1}{2},\frac{-1}{2},\frac{-1}{2},0,0,\dots,0) \\
\Psi_{2,2} &= (0,0,0,0,\frac{1}{2},\frac{1}{2},\frac{-1}{2},\frac{-1}{2},\dots,0) \\
&\vdots \\
\Psi_{2,N/4} &= (0,0,\dots,0,\frac{1}{2},\frac{1}{2},\frac{-1}{2},\frac{-1}{2})
\end{aligned} \tag{4.10}$$

The scaling functions are Φ_{m}^{2},

$$\begin{aligned}
\Phi_{1,1} &= (\frac{1}{2},\frac{1}{2},\frac{1}{2},\frac{1}{2},0,0,\dots,0) \\
\Phi_{1,2} &= (0,0,\frac{1}{2},\frac{1}{2},\frac{1}{2},\frac{1}{2},\dots,0) \\
&\vdots \\
\Phi_{1,N/2} &= (0,0,\dots,\frac{1}{2},\frac{1}{2},\frac{1}{2},\frac{1}{2})
\end{aligned} \tag{4.11}$$

When the Haar wavelet transform is applied onto an image, we can get the low-frequency image and high-frequency components in the horizontal, vertical and diagonal directions for different levels as described in the equation (4.3). The different levels are corresponding to the different frequency or resolution.

Figure 4.4 is the Haar wavelet coefficients for pattern image for level 1 to level 4 at horizontal and vertical direction. Based on the cross-pattern resolution, we choose level 4 for the contrast ratio calculation.

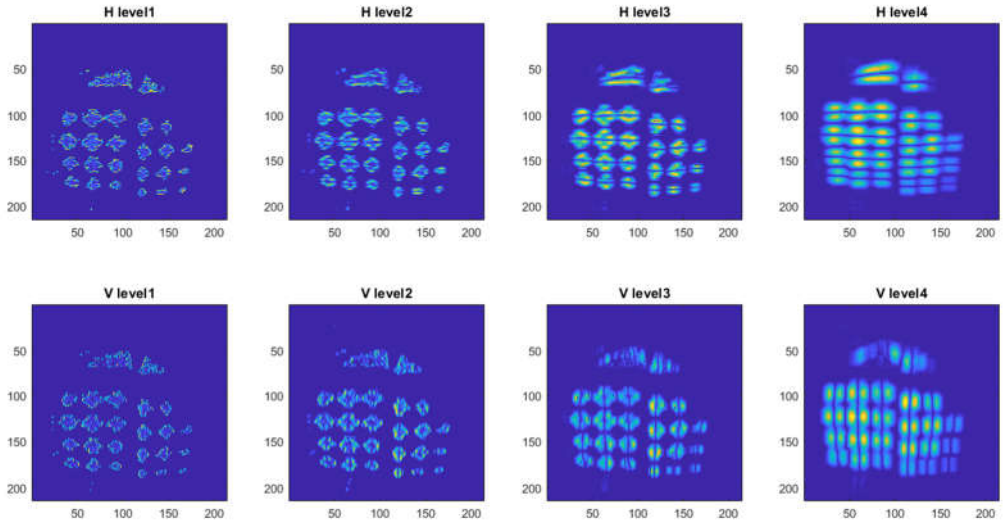

Figure 4.4 Haar wavelet coefficients for pattern image for level 1 to level 4 at the horizontal and vertical direction

4.2.3 Watershed Image Segmentation

Image segmentation is the image process of dividing an image into multiple parts. We apply the image segmentation on the pattern image to identify the area of each cross in this image. There are serval ways to perform image segmentation such as thresholding methods, color-based segmentation, transform methods and texture methods.

In this experiment, both the thresholding method and transform method are promising. We choose the transform methods and use the watershed transform to implement the processing for simplicity. The watershed transform works on the grayscale image. It finds "catchment basins" or "watershed ridge lines" in an image by treating it as a where light pixel represent high elevations, and dark pixels represent low elevations. [43] Then label all the watershed region from 1 to the number of the watershed region. In this application, we use watershed transform to divide all the crosses region (Figure 4.5 Left) and multiply with the binary pattern image to find the area of each cross object in the pattern image and label it with its index number (Figure 4.5 right).

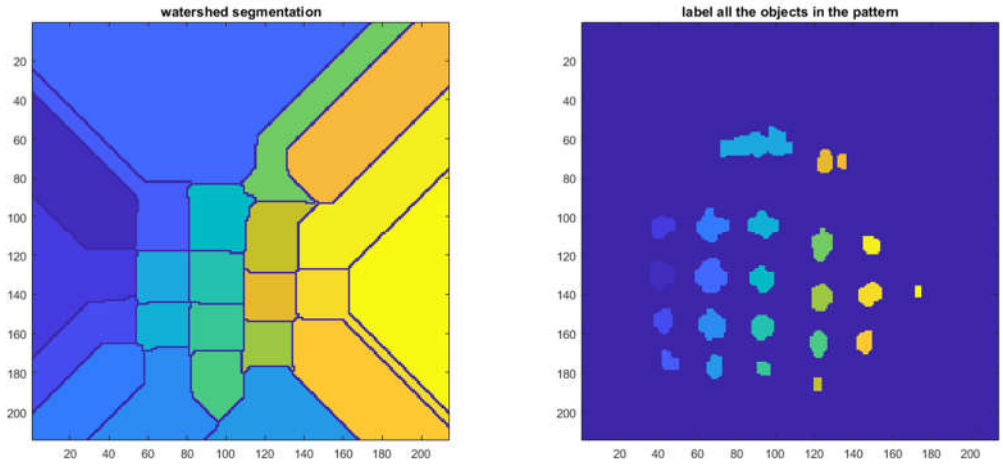

Figure 4.5 The segmentation of the pattern image (left)

and labelled pattern image by the segmentation result (right)

4.2.4 Result Analysis

For each cross in the pattern, we assign the contrast ratio result from the Haar wavelet coefficients into its corresponding area. Figure 4.6 is the contrast ratio map. A test scene is a step object. The height for its left part is different with the right part. In the contrast ratio map, we can tell the contrast ratio for the left part is in the range [0.7 1.1], the contrast ratio for the right part is in the range [0.98 1.2]. Figure 4.7 is the box plot of the contrast ratio value of the crosses on the left and right side of the step object. In each box, there are five numbers to present a set of data. The central mark shows the median, and the bottom and top edges of the box indicate the 25th and 75th percentiles, respectively. [44] There is a noticeable difference for the contrast ratio between the left and right side. However there is still some overlap range. The question needs to be answered is whether there is a significant difference or only random difference between the two contrast ratio data sets.

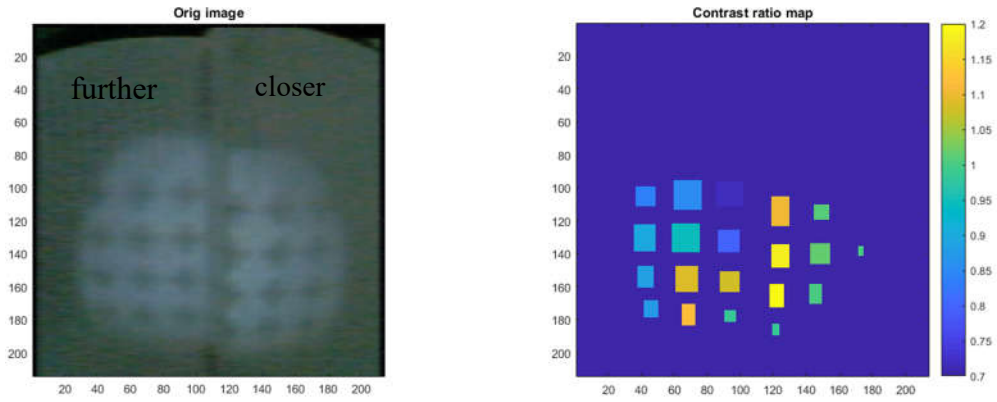

(a) (b)

Figure 4.6 (a) is the original image by capturing the test object with cross pattern projection (b) is the depth map

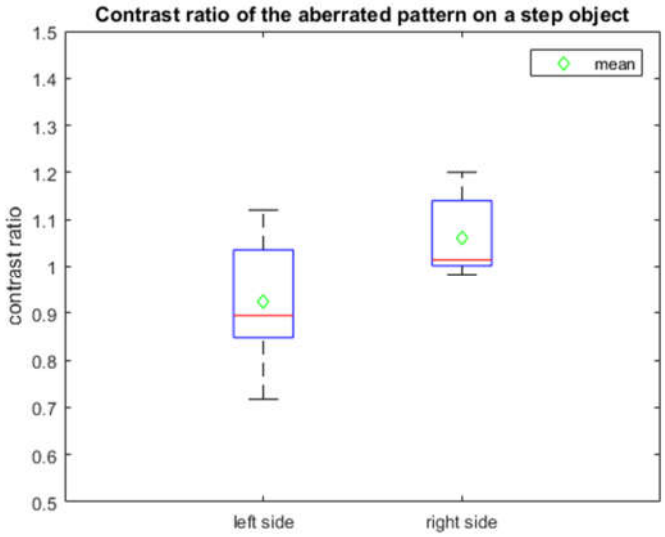

Figure 4.7The contrast ratio values of the crosses pattern at the left and right side of the step object

One of the most commonly used hypothesis test for this application is the two-sample t-test. The null hypothesis is that two independent samples data come from normal distributions have equal means. Table 4.1 is the result for 2 sample t-test. h equals to 1 means the rejection of the null hypothesis at the α ($\alpha = 5\%$ in the default MATLAB setup) significance level. p-value of the test is the probability of observing values under the null hypothesis. In this application, the contrast ratio from left side and the right side of the step object have 1.45% probability to have equal means.

Confidence interval shows with 95% confidence, the difference in contrast ratio between the left and right side is between -0.2441 and -0.0307. The T-Statistic (tstat) is the value used to produce the p-value (Prob Level) based on the T distribution. sd is the Pooled estimate of the population standard deviation.

The contrast ratio variation at the same depth is caused by the different field of the pattern and the distortion of the mini camera. We introduced the contrast ratio change caused by the different field in the simulation of chapter 2. This phenomenon exists in all the system with controlled aberration method. We can eliminate it by proper calibration across the entire field of view. However, the influence of the distortion and low resolution of the mini camera cannot be fixed. So, it is hard to get an accurate calibration for measurement. In this sense, we use this experiment to prove that at different depth the contrast ratio shows a noticeable difference. For accurate depth measurement, we use DSLR to implement the calibration and depth measurement.

Table 4.1 The Contrast ratio data analysis and 2 sample t test result

	Contrast ratio for left side	Contrast ratio for right side
Mean	0.9245	1.0619
Standard deviation	0.1244	0.0865
Standard error of the mean	0.0104	0.0108
h	1	
p	0.0145	
95% Confidence interval	[-0.2441, -0.0307]	
T-Statistic	-2.7062	
Degrees of freedom	18	
sd	0.1112	

4.3 Experiment with the on-axis DSLR

4.3.1 Calibration

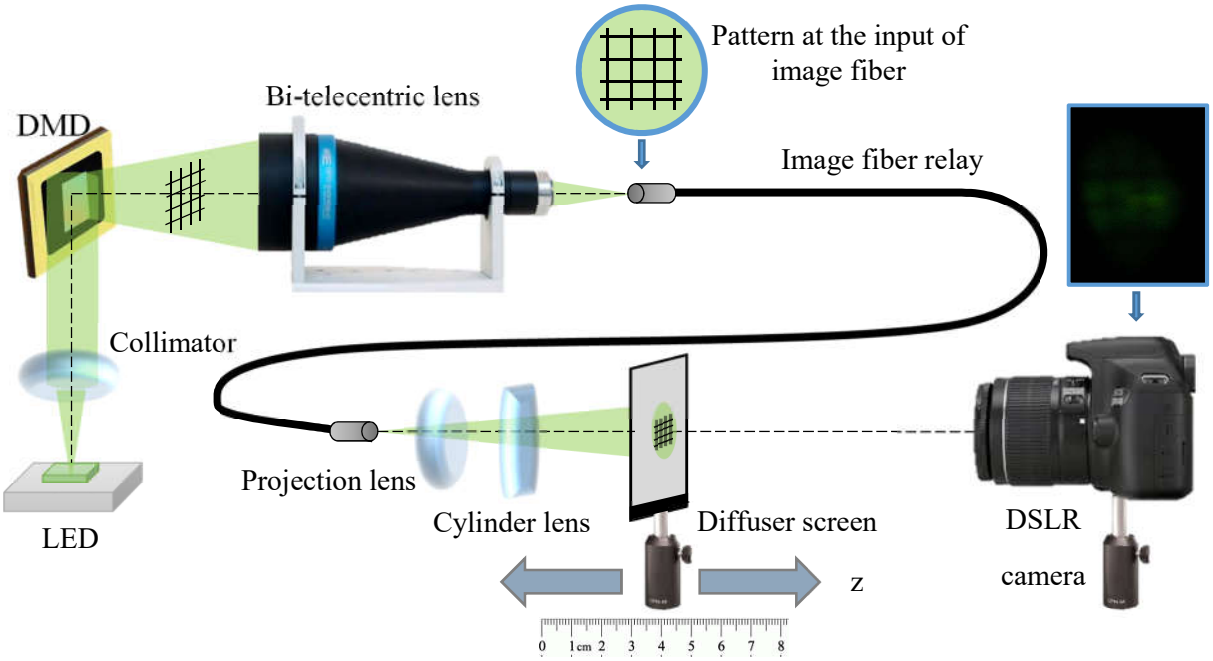

Figure 4.8 Calibration setup for depth measurement with DSLR camera

The goal of the calibration process is to find the relationship between the distance and the contrast ratio. With the calibration result, we can find out the depth information by measuring the contrast ratio of the captured image.

In chapter 2, we talked about the relationship between contrast ratio and depth in the simulation study. From the simulation, we can tell that for the same depth the contrast ratio changes at a different field. In this sense, the calibration should be done based on the different field. We noticed that the wavelength also influences the measurement. In this sense, the green laser beam is an ideal choice for illimitation. However, for simplicity, we use green light LED in this experiment.

Figure 4.8 shows the calibration setup for this experiment. The illumination path is constructed with the LED, DMD chip, bi-telecentric coupling lens, image fiber relay and projection system with astigmatism. The details of the illumination path design were discussed in chapter 3.

The collimated green light incident into the DMD chip and be modulated with the projection pattern. This modulated beam is focused by a bi-telecentric lens to form the intermediate pattern

image into the image fiber. The image fiber relay carries this pattern into the distal tip of the illumination path, and this is projected with astigmatism onto the diffuser screen. Then the on-axis imaging path captures the transmitted image through the screen for the further calibration data processing.

For simplicity, the DSLR camera works as the imaging path. We place the DSLR camera behind the diffuser screen to capture the transmitted image to keep the illumination path and image path coaxial. In the future work, for practical endoscope design, the imaging path should be on the same side of the illumination path to capture the reflected image of test scene.

4.3.1.1 Calibration Data Processing

In this calibration data processing, we measure the contrast ratio based on the different field in the captured image at the different depth. Figure 4.10 is the calibration image captured with the diffuser screen at 8mm. (a) is the pattern image ; (b) is the background image ; (c) is the pattern image divided by the background image. This processing is applied to eliminate the non-uniformity of the illumination. (d) is the smoothed sampling data extracted from the vertical and horizontal lines in (c).

For the contrast calculation, we extract the data from the nine sampling lines in Figure 4.9 (c). The captured image intensity is noisy due to the diffuser screen. So, in the data processing, we smooth the sampling data first then use the peak and valley value to calculate the Michelson contrast for each field. We can draw the vertical contrast in each field by applying this data processing for all the vertical sampling lines. Then apply the same calculation for the horizontal sampling data which gives the horizontal contrast for each field. Then use the horizontal contrast divide the vertical contrast to get the contrast ratio for each field.

In Figure 4.9 (c), we labeled nine areas which centered at the crosses of the sampling data line as area 1 to 9. The area 5 is the center field of the projection, area 2, 4, 6,8 are the middle fields the area 1,3,7,9 are the outer field. For the ideal condition, the contrast ratio in each field should be

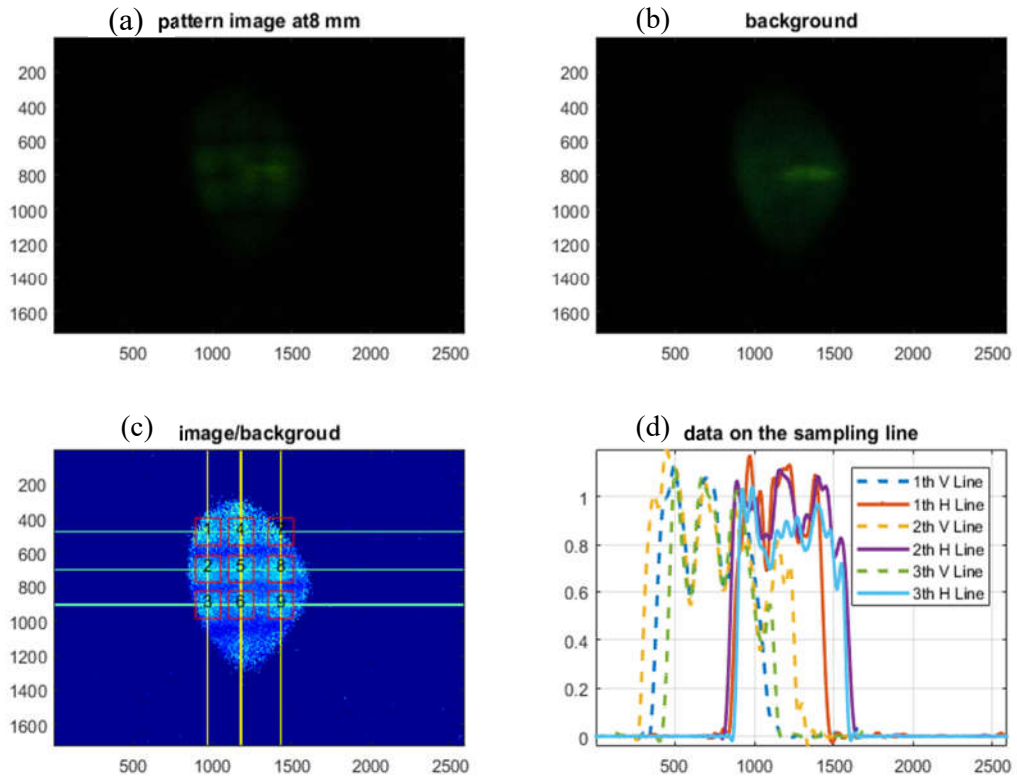

Figure 4.9 Calibration data with screen at 8 mm

constant. In another word, the middle fields share the same calibration result; the outer fields have the same calibration result.

4.3.1.2 Calibration Result and Analysis

In the section 4.3.1.1, we showed the contrast ratio calculation method for each field labeled as 1 to 9 in figure 4.9. We can get the contrast ratio vs. distance result for each field by applying this method to the calibration image at a different distance. (Figure 4.10)

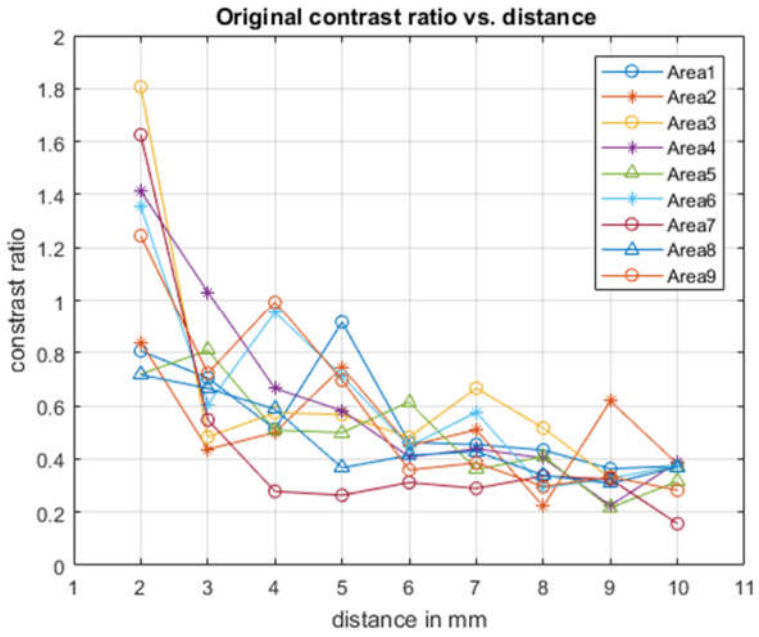

Figure 4.10 Contrast ratio vs. distance for the all the areas labeled in figure 4.9

Notice that the contrast ratio plot in Figure 4.10 is fluctuating. There are several reasons could lead to this problem: For example, the image on the diffuser screen is noisy; the illumination is not uniform. Use non-linear regression exponential decay equation model to fit a calibration curve. [45] The exponential decay equation model is:

$$Y = (Y_0 - Plateau) \cdot \exp(-K \cdot X) + Plateau \tag{4.12}$$

The fitting result is in table 4.2. Y_0 is the Y value when X is zeros, Plateau is the Y value at infinite times. K is the frequency constant. Tau is the reciprocal of K. Half- life is calculated as $\ln(2)/K$. Span is the difference between Y_0 and Plateau. A high R^2 tells that the model fit the data well. Sy.x is the standard deviation of the residuals.

Table 4.2 The non-linear regression fitting result for one decay exponential equation

	Best-fit values	Std. Error	95% CI (profile likelihood)	Goodness of Fit	
Y_0	2.824	0.7109	1.708 to 6.552	**Degrees of Freedom**	78
Plateau	0.3626	0.04223	0.2298 to 0.4443	R^2	0.6068
K	0.5849	0.1337	0.3143 to 1.04	**Absolute Sum of squares**	3.028
Half Life	1.185		0.6666 to 2.206	**Sy.x**	0.197
Tau	1.71		0.9618 to 3.182	**Constraints**	
Span	2.461	0.6858		**K**	K > 0

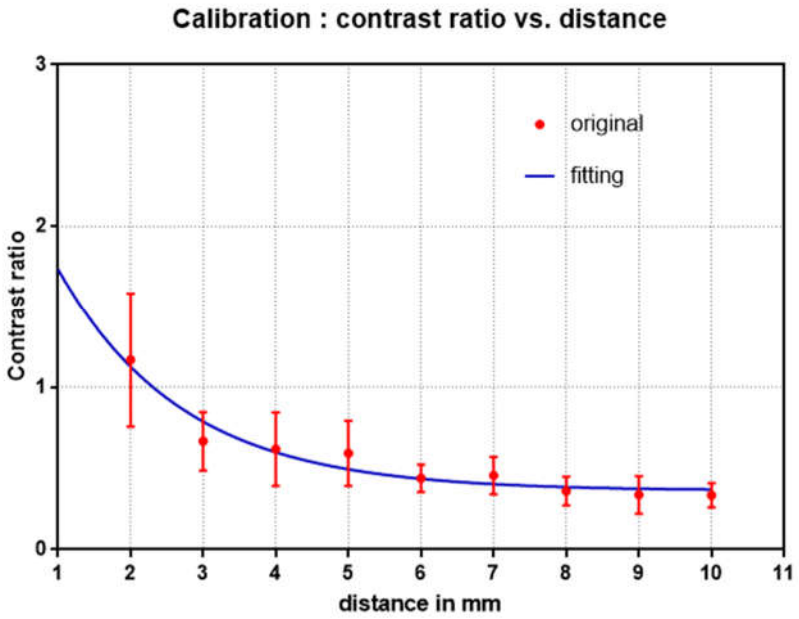

Figure 4.11 Calibration result with error bar

Figure 4.11 is the final calibration result with the non-linear regression. The blue line is the fitting result, and the red line shows the means value with error bar as the standard deviation.

4.3.2 Depth Measurement

4.3.2.1 Set-up

In the depth measurement process, the illumination and imaging path set up are the same as the calibration setup; then the only difference is changing the diffuser screen into two separate pieces with different distance. Figure 4.12 shows an example of the depth experiment configuration. We can change the object depth by shifting the left and right diffuser screen location. The distance between the left screen and the right screen is approximately 1 mm corresponding to the test scene in figure 4.13.

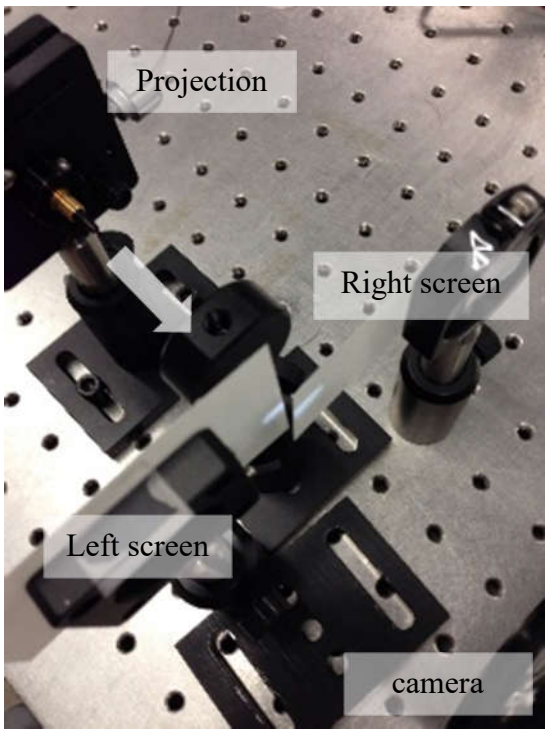

Figure 4.12Separated diffuser screen as test scene

4.3.2.2 Test Image and data process

Figure 4.13 is the image of the test scene. The contrast calculation method is the same as the contrast calculation in the calibration processing. The test scene is two separated screens on the left and right side with a different distance. In this sense, use the contrast ratio at area 1,2,3 for the

left screen and the contrast ratio at area 7,8,9 for the right screen. The contrast ratio values for the area 1 to 3 and 7 to 9 are shown in table 4.3.

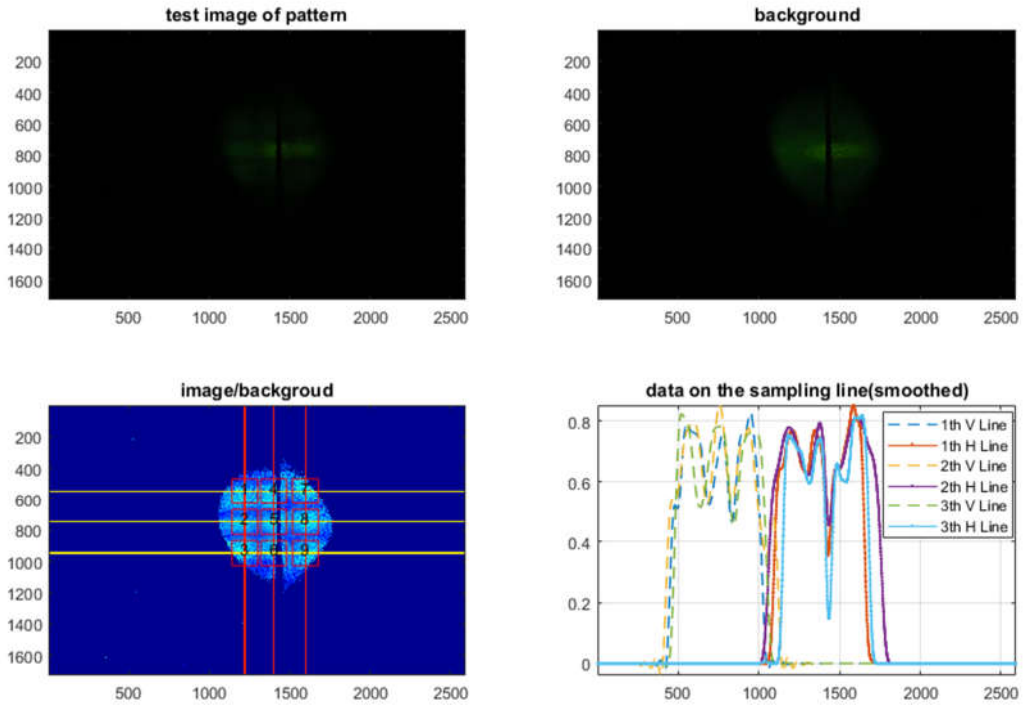

Figure 4.13 Image for the test scene

Table 4.3 Contrast ratio in measurement

Area (on the left side)	Contrast Ratio	Area (on the right side)	Contrast Ratio
1	0.6798	7	0.5980
2	0.5677	8	0.4994
3	0.5682	9	0.5515

With the measured contrast ratio, interpolate the calibration result. Then the distances of the left screen and right screen are shown in table 4.4. Figure 4.14 shows the mean value with CI 95% limit of the depth information of the test screen.

Table 4.4 Measured depth information

Distance in mm	Mean	Upper limit (CI 95%)	Lower limit (CI 95%)
Left screen	3.961	4.546	3.459
Right screen	4.405	5.083	3.790

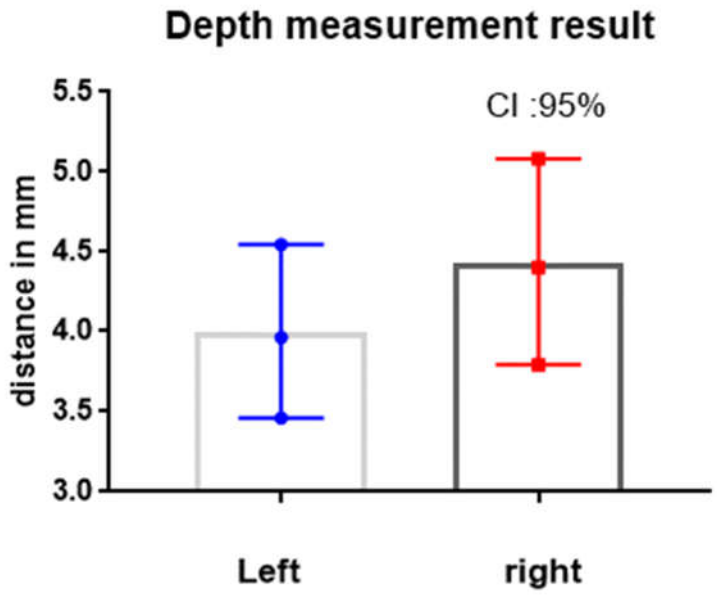

Figure 4.14Depth measurement result

4.3.2.3 Error Analysis

Figure 4.14 shows the depth measurement result. The difference of the distance mean value between the left and right screen is 0.444 mm. In 95% confidence interval, the distance from the left screen to the right screen is in the range of - 0.7560 mm to 1.6240 mm. The experiment setup 1 mm is in between of the range.

There are several factors which might lead to the measurement error. Those factors should be eliminated in the future measurement. From the hardware point of view. in both the calibration and measurement processing, the test image with the aberrated pattern on the diffuser screen is

noisy. However, the actual organ images are much smoother than the image in this experiment. To deal with this problem, we need to design a new imaging path for the endoscope to capture the reflected image. Based on the new setup, we do not need to use the diffuser screen anymore; we can use the object with the similar BRDF as the organ.

Another problem is the mounting for the diffuser screen in calibration processing, the screen might be tilted, and it is not entirely flat. We can solve this problem by better mounting in the future work.

From the data processing point of view, the sampling lines in the test image were chosen by hand. Use one sampling line for contrast calculation might not be accurate for the same field, and this processing is also not applicable for the actual measurement. In this sense, the better data processing should be developed for the contrast ratio calculation.

4.4 Conclusion

In this chapter, I talked about the controlled aberration depth measurement experiment with the miniature camera and the on-axis DSLR camera with diffuser screens. Due to the high distortion of the mini camera, it is hard to implement an accurate depth measurement with this configuration. So, the goal of this experiment is to check whether the contrast ratio changes significantly for the different depth. The Haar wavelet coefficients were used to calculate the contrast of the aberrated crosses pattern. The two-sample t-test result shows that the contrast ratio from the left side and the right side of the step object have 1.45% probability to have equal means.

In the on-axis DSLR experiment, the imaging path is a DSLR camera placed on-axis to capture the transmitted image on the diffuser screen. The DSLR camera can overcome the low resolution and high distortion problem in the mini camera configuration. The actual application in endoscope the image path should compact enough and be placed on the same side of the illumination path. The calibration was implemented by shifting the screen along the axis and measuring the contrast ratio for all the fields. Based on the one-decay exponential non-linear regression, we fit a

calibration curve and use the interpolation to measure the depth of two separated diffuser screen. The distance of left screen is 3.961 mm (95%CI: 3.459 mm, 4.546 mm). The distance to the right screen is 4.405 mm (95%CI: 3.790 mm, 5.083 mm).

CHAPTER 5

FUTURE WORK AND CONCLUSION

5.1 Future work

In this thesis, the experiments were conducted on the controlled aberration endoscope prototype. The illumination path in this prototype uses the image fiber as the relay system. The cylinder lens is placed at the tip of the illumination. The imaging path in the prototype is a miniature camera or on-axis DSLR.

The controlled aberration depth measurement method does not require the angle diversity. In this prototype, the cylinder lens is located at the tip of the illumination path, so it is hard to reuse the illumination path as the imaging path. Hence, the miniature camera was used as the imaging path. However the distortion in the miniature camera is too high, so it is hard to achieve the accurate calibration based on the mini camera configuration. The on-axis DSLR configuration could deal with the high distortion problem, but the DSLR captures the transmitted image, so this structure is not applicable to the actual endoscope.

In the future work, there are serval directions deserve to explore to improve the performance of controlled aberration endoscope prototype. Those works include the new optical design and new computational method.

We can achieve a uniaxial controlled aberration endoscope configuration by combining the illumination path and imaging path with a beam splitter. The illumination path is constructed with the light source (pattern display), a coupling lens, the relay system and the projection lens and a cylinder lens. The imaging path in the conventional endoscope is constructed with the objective lens, relay system, focusing lens and the sensor. In this sense, the projection lens can be used as the objective lens for imaging and the coupling lens can be used as the focusing lens. The cylinder lens should be placed between the light source and beam splitter. So, the cylinder lens will not allow influent the imaging path. The light passes the cylinder lens before the relay system. In this sense, the image fiber bundle might not be sufficient to be the relay system to retain the aberrated

wavefront. In the future design, we can consider using the rod lens relay or GRIN lens relay in the prototype.

Another direction to improve the performance is based on the computational method. For example, projecting multiple patterns and shift the pattern location could increase the depth map spatial resolution. In chapter 4, we showed the experiment with the crosses as projection pattern. The depth map spatial resolution is determined by the cross-pattern resolution. In this sense, if we shift the pattern spatially to create a series of the shifted pattern and project those patterns on the test scene and implement the corresponding depth map calculation, we could get a depth map sequence. Then combine all the depth map into one depth map could increase the depth map spatial resolution. This method presents a trade-off between time and spatial resolution; it requires a static or a slowly changed test scene.

5.2 Conclusion

In this thesis, chapter 1 focuses on the motivation of implementing the controlled aberration endoscope. The first part is the primary endoscopic system and its history. Then introduce the rigid endoscope with conventional relay lens or rod lens or GRIN lens as the relay system and the flexible endoscope with the image fiber as the relay system. After that, the specifications of the commercial endoscopes were listed; Since the 2D endoscope only offer image sequence without depth information. It is necessary to develop 3D endoscope to help the surgeons rebuild the test scene more accurately. Then the comparison study about the performance of 2D and 3D endoscopes proves that the 3D endoscopes have better performance than the 2D endoscope.

The literature review about the 3D imaging method which could be applied to the endoscopic system was presented afterward. The stereo and structured light method are commonly used for depth measurement; but, both of those two methods requires the angle diversity. The Time-of-Flight method is promising over a long distance. However the ToF camera is costly, and it cannot retain the high-resolution 2D image. The defocus method is uniaxial and could keep same optical design, but it limited to measuring the low contrast scene. Then I introduced the concept of the

controlled aberration for depth measurement. This method only requires the projection pattern and differential focus. It could overcome the problems in another 3D imaging methods.

Chapter 2 is about the simulation of the endoscope scale projection lens with a cylinder lens. The simulation result shows that the controlled aberration method can be applied to the endoscope system. This simulation result works as reference information in the prototype design.

Chapter 3 focuses on the controlled aberration endoscope prototype design. The illumination path is constructed with a LED light source and DMD chip to modulate the projection pattern; The bi-telecentric lens creates an intermediate image into the image fiber relay system then the pattern is projected onto the test scene through a projection lens and cylinder lens. The imaging path could be the 2D imaging path, for simplicity, we choose the miniature camera or the DSLR camera to prove the concept.

In chapter 4, the depth measurement experiments based on the mini camera ad on-axis DSLR was conducted. Due to the high distortion of the mini camera, this set-up cannot achieve accurate calibration. Hence it is hard to use this set-up for depth measurement. In this sense, we use this setup to project a pattern on a step object, by measuring the contrast ratio on the step object with different height, we can tell that there is signification contrast ratio change at a different distance. The on-axis DSLR configuration uses the diffuser screens as the “detector,” and the DSLR camera only captures the screen for image. The first part is the calibration process; then the second part is a measurement of a step object constructed by two separated diffuser screens. The distance of left screen is 3.961 mm (95%CI: 3.459 mm, 4.546 mm). The distance of the right screen is 4.405 mm (95%CI: 3.790 mm, 5.083 mm). The actual separation between this two screens is around 1 mm.

In this thesis, the main contribution is that I proved that the controlled aberration method is applicable in the endoscopic scale and then designed and implemented a controlled aberration endoscope prototype and conducted depth measurement experiment on the prototype. In the future work, the new optical design or the new computational processing might contribute to improving the performance of the controlled aberration endoscope.

APPENDIX A-SUPPLEMENTARY DATA

.

	Surf:Type		Comment	Radius	Thickness	Material	Coating	Semi-Diameter	Chip Zone
0	OBJECT	Standard		Infinity	0.000			0.100	0.000
1	(aper)	Gradient 5	IFRL-100-XXX-50	Infinity	2.490	GTAG		0.500 U	-
2	STOP (aper)	Standard		Infinity	3.606 V			0.500 U	0.000
3	(aper)	Standard		16.608	1.100	B270		3.200 U	0.000
4	(aper)	Standard		-16.608 P	4.193 V			3.200 U	0.000
5	(aper)	Toroidal	47760	4.130	2.000	BK7	ZEC_MF550	2.500 U	-
6	(aper)	Standard		Infinity	1.183 M			2.500 U	0.000
7		Standard		Infinity	0.950			0.723	0.000
8	IMAGE	Standard		Infinity	-			0.707	0.000

Figure 1. The simulation lens data in chapter 2

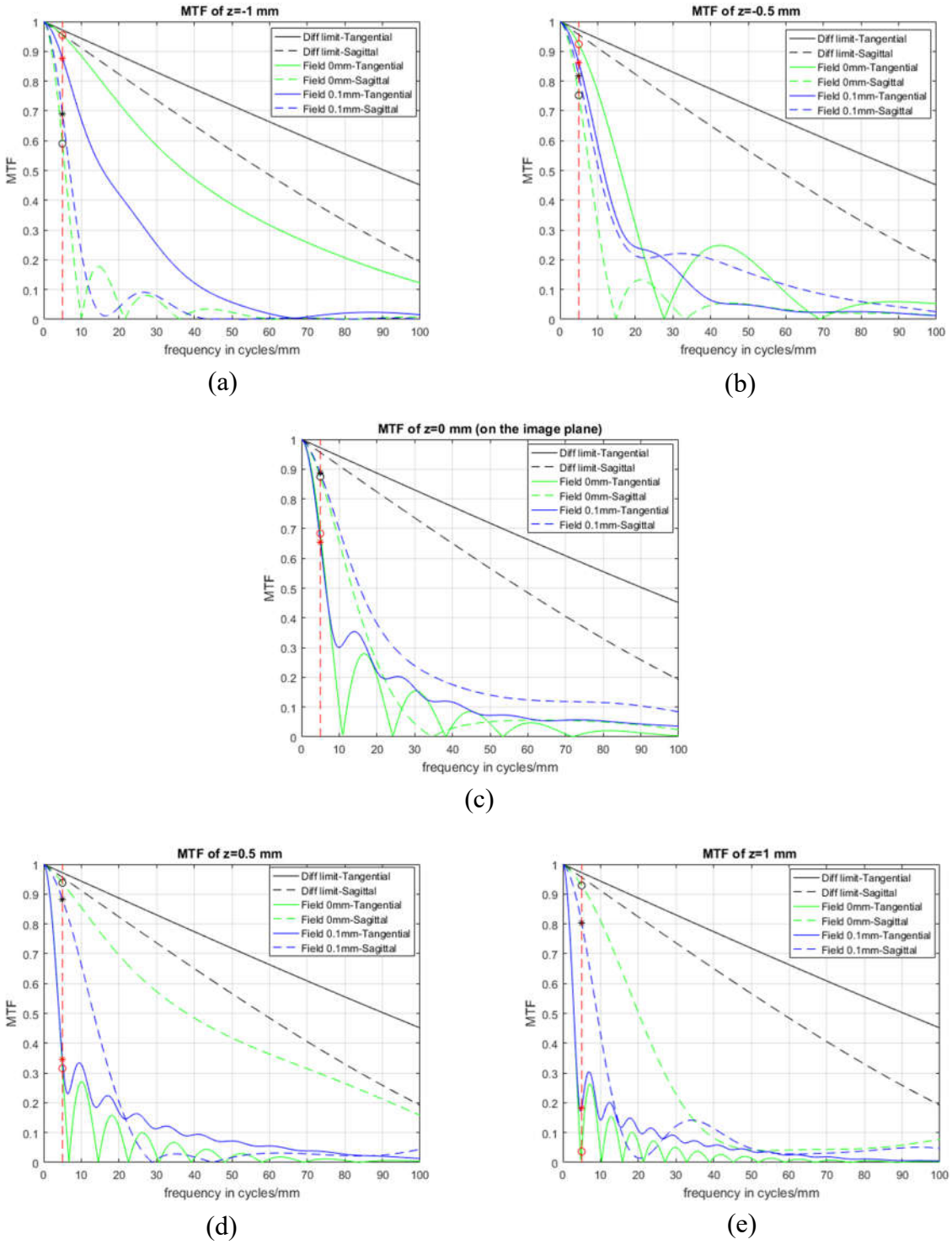

Figure 2. The MTF for tangential and sagittal direction for the test plane at a different distance

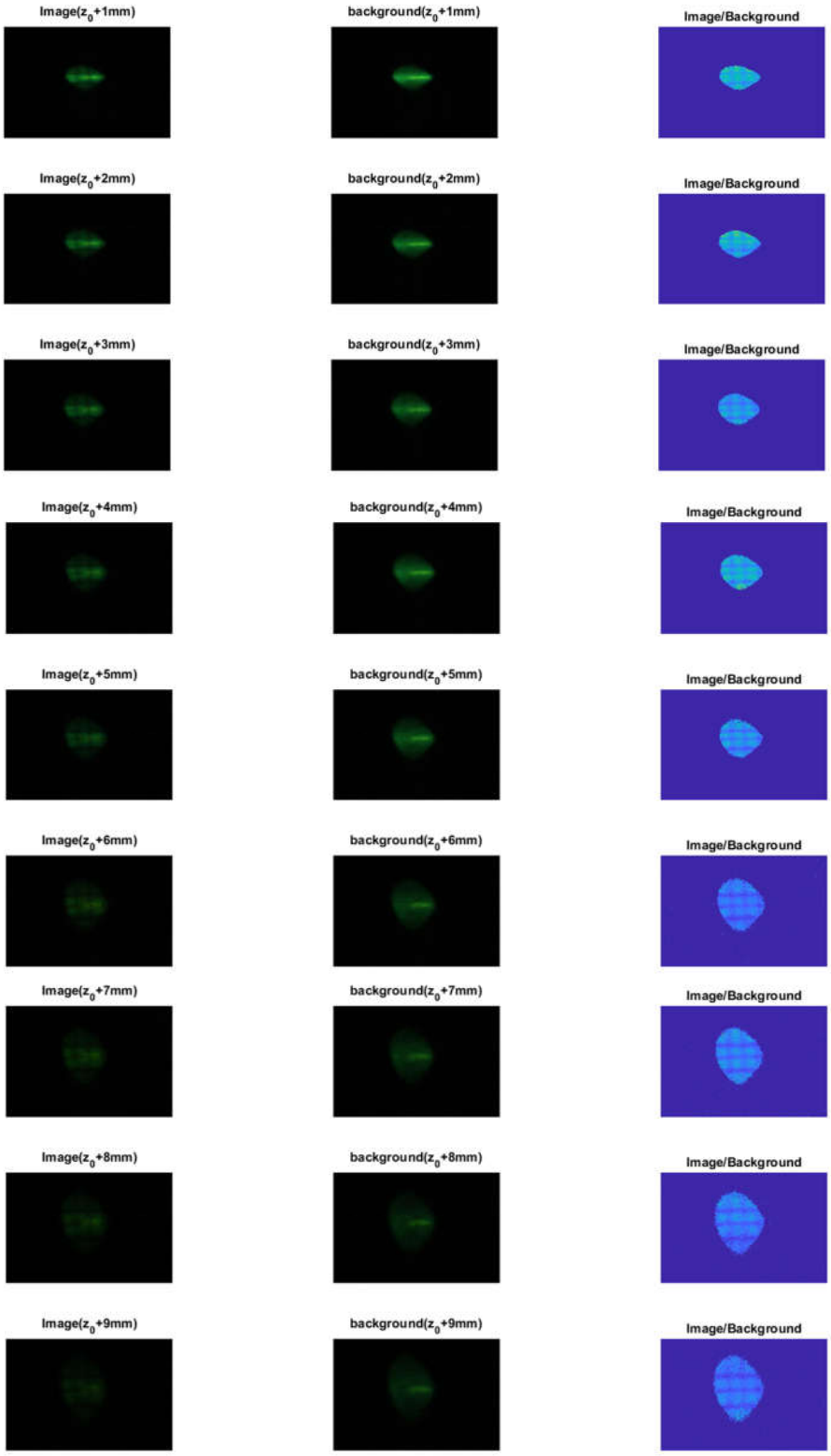

Figure 3. Calibration images in chapter 5

REFERENCE

1. R. Bogdanova, P. Boulanger, and B. Zheng, "Depth Perception of Surgeons in Minimally Invasive Surgery," Surgical Innovation **23,** 515-524 (2016).

2. J. Shah, "Endoscopy through the ages," BJU International **89,** 645-652 (2002).

3. P. C. De Groen, "History of the Endoscope [Scanning Our Past]," JPROC **105,** 1987-1995 (2017).

4. B. I. Hirschowitz, "A personal history of the fiberscope," Gastroenterology **76,** 864-869 (1979).

5. Hopkins Harold Horace, "Optical system having cylindrical rod-like lenses," **US3257902A,** (1960).

6. A. J. DiMarino and S. B. Benjamin 1948, *Gastrointestinal disease: an endoscopic approach* (Blackwell Science, 1997).

7. D. C. Leiner, *Digital Endoscope Design* (International Society for Optics and Photonics SPIE, 2015).

8. GRINTECH, "GRIN LENSES AND LENS SYSTEMS FOR IMAGING OPTICS," http://www.grintech.de/grin-lenses-and-lens-systems-for-imaging-optics.html.

9. R. Liang and Society of Photo-optical Instrumentation Engineers, *Optical design for biomedical imaging* (SPIE, 2010).

10. Olympus, "GIF-HQ190," http://medical.olympusamerica.com/sites/us/files/pdf/GIF-HQ190_OAIGI0312BRO8801_1.pdf.

11. L. W. Way, L. Stewart, W. Gantert, K. Liu, C. M. Lee, K. Whang, and J. G. Hunter, "Causes and prevention of laparoscopic bile duct injuries - Analysis of 252 cases from a human factors and cognitive psychology perspective," Ann. Surg. **237,** 460-469 (2003).

12. Intuitive Surgical, "Intuitive Surgical - da Vinci Surgical System," https://www.intuitivesurgical.com/products/davinci_surgical_system/.

13. S. Kong, B. Oh, H. Yoon, H. S. Ahn, H. Lee, S. G. Chung, N. Shiraishi, S. Kitano, and H. Yang, "Comparison of two- and three-dimensional camera systems in laparoscopic performance: a novel 3D system with one camera," Surgical endoscopy **24,** 1132-1143 (2010).

14. P. Storz, G. Buess, W. Kunert, and A. Kirschniak, "3D HD versus 2D HD: surgical task efficiency in standardised phantom tasks," Surg Endosc **26,** 1454-1460 (2012).

15. T. Usta, T. Karacan, M. Naki, A. Calık, L. Turkgeldi, and V. Kasimogullari, "Comparison of 3-dimensional versus 2-dimensional laparoscopic vision system in total laparoscopic hysterectomy: a retrospective study," Arch Gynecol Obstet **290,** 705-709 (2014).

16. R. Smith, K. Schwab, A. Day, T. Rockall, K. Ballard, M. Bailey, and I. Jourdan, "Effect of passive polarizing three-dimensional displays on surgical performance for experienced laparoscopic surgeons," British Journal of Surgery **101,** 1453-1459 (2014).

17. B. Alaraimi, W. El Bakbak, S. Sarker, S. Makkiyah, A. Al-Marzouq, R. Goriparthi, A. Bouhelal, V. Quan, and B. Patel, "A Randomized Prospective Study Comparing Acquisition of Laparoscopic Skills in Three-Dimensional (3D) vs. Two-Dimensional (2D) Laparoscopy," World J Surg **38,** 2746-2752 (2014).

18. A. Lusch, P. L. Bucur, A. D. Menhadji, Z. Okhunov, M. A. Liss, A. Perez-Lanzac, E. M. McDougall, and J. Landman, "Evaluation of the Impact of Three-Dimensional Vision on Laparoscopic Performance," Journal of Endourology **28,** 261-266 (2013).

19. Y. S. Tanagho, G. L. Andriole, A. G. Paradis, K. M. Madison, G. S. Sandhu, J. E. Varela, and B. M. Benway, "2D Versus 3D Visualization: Impact on Laparoscopic Proficiency Using the Fundamentals of Laparoscopic Surgery Skill Set," Journal of Laparoendoscopic & Advanced Surgical Techniques **22,** 865-870 (2012).

20. P. Honeck, G. Wendt-Nordahl, J. Rassweiler, and T. Knoll, "Three-Dimensional Laparoscopic Imaging Improves Surgical Performance on Standardized Ex-Vivo Laparoscopic Tasks," Journal of Endourology **26,** 1085-1088 (2012).

21. J. K. Y. Ko, R. H. W. Li, and V. Y. T. Cheung, "Two-Dimensional Versus Three-Dimensional Laparoscopy: Evaluation of Physicians' Performance and Preference Using a Pelvic Trainer," Journal of Minimally Invasive Gynecology **22,** 421-427 (2015).

22. E. Gómez-Gómez, J. Carrasco-Valiente, J. Valero-Rosa, J. P. Campos-Hernández, F. J. Anglada-Curado, J. L. Carazo-Carazo, P. Font-Ugalde, and M. J. Requena-Tapia, "Impact of 3D vision on mental workload and laparoscopic performance in inexperienced subjects," Actas Urológicas Españolas (English Edition) **39,** 229-235 (2015).

23. M. Özsoy, P. Kallidonis, I. Kyriazis, V. Panagopoulos, M. Vasilas, G. C. Sakellaropoulos, and E. Liatsikos, "Novice surgeons: do they benefit from 3D laparoscopy?" Lasers Med Sci **30,** 1325-1333 (2015).

24. J. G. Bittner, C. A. Hathaway, and J. A. Brown, "Three-dimensional visualisation and articulating instrumentation: Impact on simulated laparoscopic tasks," Journal of Minimal Access Surgery **4,** 31 (2008).

25. J. Geng and J. Xie, "Review of 3-D Endoscopic Surface Imaging Techniques," IEEE Sensors Journal **14,** 945-960 (2014).

26. J. Batlle, E. Mouaddib, and J. Salvi, "Recent progress in coded structured light as a technique to solve the correspondence problem: a survey," Pattern Recognition **31,** 963-982 (1998).

27. N. T. Clancy, D. Stoyanov, L. Maier-Hein, A. Groch, G. Yang, and D. S. Elson, "Spectrally encoded fiber-based structured lighting probe for intraoperative 3D imaging," Biomed. Opt. Express **2,** 3119-3128 (2011).

28. Z. Song, *Handbook of 3D machine vision: optical metrology and imaging* (CRC Press, 2016).

29. R. Horaud, M. Hansard, G. Evangelidis, and C. Ménier, "An overview of depth cameras and range scanners based on time-of-flight technologies," Mach Vision Appl **27,** 1005-1020 (2016).

30. J. Penne, K. Höller, M. Stürmer, T. Schrauder, A. Schneider, R. Engelbrecht, H. Feußner, B. Schmauss, and J. Hornegger, "Time-of-Flight 3-D Endoscopy," in *Medical Image Computing and Computer-Assisted Intervention – MICCAI 2009: 12th International Conference, London, UK, September 20-24, 2009, Proceedings, Part I,* G. Yang, D. Hawkes, D. Rueckert, A. Noble, and C. Taylor, eds. (Springer Berlin Heidelberg, 2009), pp. 467-474.

31. Yukitoshi Otani, Fumio Kobayashi, Yasuhiro Mizutani, and Toru Yoshizawa, "Three-dimensional profilometry based on focus method by projecting LC grating pattern," in Anonymous (, 2009), pp. 6.

32. G. C. Birch, J. S. Tyo, and J. Schwiegerling, "Depth measurements through controlled aberrations of projected patterns," Optics express **20,** 6561 (2012).

33. Lee Benjamin, "DMD 101:
Introduction to Digital Micromirror Device (DMD)
Technology," Texas Instruments1 (2008).

34. http://www.ti.com/tool/DLPLIGHTCRAFTER, "DLPLIGHTCRAFTER DLP® LightCrafter™ Evaluation Module | TI.com," http://www.ti.com/tool/DLPLIGHTCRAFTER.

35. J. S. Walker, *A primer on wavelets and their scientific applications* (Chapman & Hall/CRC, 1999).

36. S. G. Mallat, "A theory for multiresolution signal decomposition: the wavelet representation," IEEE Trans. Pattern Anal. Mach. Intell. **11,** 674-693 (1989).

37. Jinshan Tang, Qingling Sun, and K. Agyepong, "An Image Enhancement Algorithm Based on a Contrast Measure in the Wavelet Domain for Screening Mammograms," in Anonymous (IEEE, 2007), pp. 32.

38. Y. Lai and C. -. J. Kuo, "Image quality measurement using the Haar wavelet," in Anonymous (, 1997).

39. P. Vandergheynst, M. Kutter, and S. Winkler, "Wavelet-based contrast computation and application to digital image watermarking," in Anonymous (SPIE, 2000), pp. 82-92.

40. P. S. Addison, *The Illustrated Wavelet Transform Handbook : Introductory Theory and Applications in Science, Engineering, Medicine and Finance, Second Edition* (CRC Press, 2017).

41. D. Sundararajan, *Discrete Wavelet Transform : A Signal Processing Approach* (John Wiley & Sons, Incorporated, 2015).

42. Z. K. Chen, Y. Tao, and X. Chen, "Multiresolution local contrast enhancement of x-ray images for poultry meat inspection," Appl. Opt. **40,** 1195-1200 (2001).

43. https://www.mathworks.com/help/images/ref/watershed.html, "Watershed transform - MATLAB watershed," https://www.mathworks.com/help/images/ref/watershed.html.

44. Matlab, "boxplot-MATLAB," .

45. H.J.Motulsky, ""Equation One phase decay" GraphPad Curve Fitting Guide," https://www.graphpad.com/guides/prism/7/curve-fitting/index.htm?REG_Exponential_decay_1phase.htm.